NBS TECHNICAL NOTE 1071

U.S. DEPARTMENT OF COMMERCE / National Bureau of Standards

Design and Error Analysis for the WR10 Thermal Noise Standard

NATIONAL BUREAU OF STANDARDS

The National Bureau of Standards[1] was established by an act of Congress on March 3, 1901. The Bureau's overall goal is to strengthen and advance the Nation's science and technology and facilitate their effective application for public benefit. To this end, the Bureau conducts research and provides: (1) a basis for the Nation's physical measurement system, (2) scientific and technological services for industry and government, (3) a technical basis for equity in trade, and (4) technical services to promote public safety. The Bureau's technical work is performed by the National Measurement Laboratory, the National Engineering Laboratory, and the Institute for Computer Sciences and Technology.

THE NATIONAL MEASUREMENT LABORATORY provides the national system of physical and chemical and materials measurement; coordinates the system with measurement systems of other nations and furnishes essential services leading to accurate and uniform physical and chemical measurement throughout the Nation's scientific community, industry, and commerce; conducts materials research leading to improved methods of measurement, standards, and data on the properties of materials needed by industry, commerce, educational institutions, and Government; provides advisory and research services to other Government agencies; develops, produces, and distributes Standard Reference Materials; and provides calibration services. The Laboratory consists of the following centers:

Absolute Physical Quantities[2] — Radiation Research — Chemical Physics — Analytical Chemistry — Materials Science

THE NATIONAL ENGINEERING LABORATORY provides technology and technical services to the public and private sectors to address national needs and to solve national problems; conducts research in engineering and applied science in support of these efforts; builds and maintains competence in the necessary disciplines required to carry out this research and technical service; develops engineering data and measurement capabilities; provides engineering measurement traceability services; develops test methods and proposes engineering standards and code changes; develops and proposes new engineering practices; and develops and improves mechanisms to transfer results of its research to the ultimate user. The Laboratory consists of the following centers:

Applied Mathematics — Electronics and Electrical Engineering[2] — Manufacturing Engineering — Building Technology — Fire Research — Chemical Engineering[2]

THE INSTITUTE FOR COMPUTER SCIENCES AND TECHNOLOGY conducts research and provides scientific and technical services to aid Federal agencies in the selection, acquisition, application, and use of computer technology to improve effectiveness and economy in Government operations in accordance with Public Law 89-306 (40 U.S.C. 759), relevant Executive Orders, and other directives; carries out this mission by managing the Federal Information Processing Standards Program, developing Federal ADP standards guidelines, and managing Federal participation in ADP voluntary standardization activities; provides scientific and technological advisory services and assistance to Federal agencies; and provides the technical foundation for computer-related policies of the Federal Government. The Institute consists of the following centers:

Programming Science and Technology — Computer Systems Engineering.

[1]Headquarters and Laboratories at Gaithersburg, MD, unless otherwise noted; mailing address Washington, DC 20234.
[2]Some divisions within the center are located at Boulder, CO 80303.

Design and Error Analysis for the WR10 Thermal Noise Standard

William C. Daywitt

Electromagnetic Fields Division
National Engineering Laboratory
National Bureau of Standards
U.S. Department of Commerce
Boulder, Colorado 80303

U.S. DEPARTMENT OF COMMERCE, Malcolm Baldrige, Secretary

NATIONAL BUREAU OF STANDARDS, Ernest Ambler, Director

Issued December 1983

National Bureau of Standards Technical Note 1071
Natl. Bur. Stand. (U.S.), Tech Note 1071, 45 pages (Dec. 1983)
CODEN: NBTNAE

U.S. GOVERNMENT PRINTING OFFICE
WASHINGTON: 1983

CONTENTS

Design and Error Analysis for the WR10 Thermal Noise Standard

William C. Daywitt

Electromagnetic Fields Division
National Bureau of Standards
Boulder, Colorado 80303

This note describes the design and error analysis of a WR10 thermal noise power standard. The standard is designed to operate at the boiling point of liquid nitrogen with a noise temperature accurate to ± 1 K.

Key words: antenna efficiency; diffraction; error analysis; millimeter wave; noise standard; plane-wave scattering matrix.

1. Introduction

Over the past twenty years, the Electromagnetic Fields Division of the National Bureau of Standards (NBS) has built a number of coaxial and waveguide noise sources [1-3] consisting of single-mode, uniform transmission lines terminated in reflectionless loads. The accuracy of their calculated noise temperatures is typically 1% which tends to degrade as the operating frequency increases. The basic design is illustrated in figure 1 where the termination and a portion of the transmission line are immersed in a thermal reservoir at temperature T_m, with the remaining portion of the line leading to the output connector at room temperature T_o. The temperature distribution T_x of the line is also illustrated where the room-temperature portion of the line has a length ℓ. Radiation from the termination and the dissipative losses of the line result in a noise temperature

$$T_n = T_m + \Delta T \tag{1}$$

where, for the idealized distribution shown,

$$\Delta T \doteq (2a'\ell)\ (T_o - T_m). \tag{2}$$

The attenuation coefficient a' refers to the line at T_o, and the equations indicate that only that portion of the line contributes to the excess (in excess of thermal equilibrium conditions) noise temperature ΔT.

The largest source of error in calculating the noise temperature by eq (1) is the attenuation $2a'\ell$, which is usually estimated to an error varying from 10% to 20%. With this large an error, it is necessary to keep the attenuation small (to maintain the error in T_n less than 1%), implying either a small attenuation coefficient a', a short transition length ℓ, or both. In the microwave frequency range and below, the attenuation can be kept down with relatively simple engineering designs; but as the frequency increases into the millimeter-wave range, this becomes more of a problem [3]. In this higher frequency range, surface roughness also plays a bigger role [4], causing an additional increase in the attenuation.

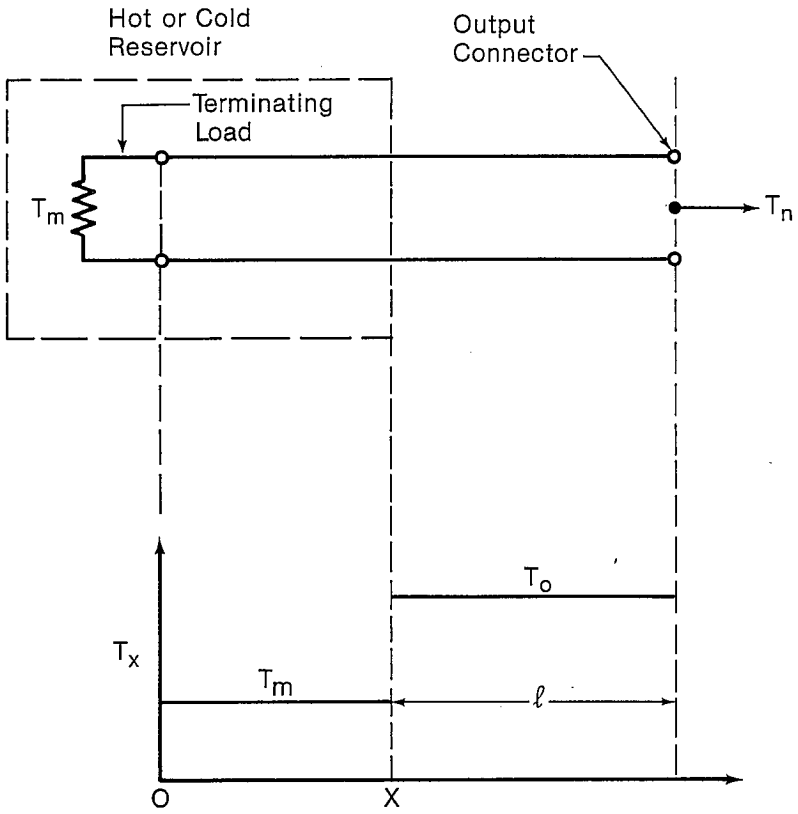

Figure 1. Schematic diagram of a transmission-line type noise standard.

To circumvent the engineering difficulties, it was decided to abandon the transmission-line type of noise standard in favor of a design incorporating a millimeter-wave horn antenna "looking" at an absorber of known temperature. The resulting antenna noise temperature is close to the measured temperature T_m of the absorber, with additional noise contributions from the dissipative antenna losses, and from the antenna side and back lobes. This type of noise source is not new, but its use as a primary reference standard of high accuracy required the successful resolution of two previously unanswered questions: can a useful expression for the noise efficiency (defined in Appendix A) of the antenna with sources in its radiating near field [5] be found; and can the error caused by near-field excess radiation (in excess of thermal-equilibrium conditions) entering the side and back lobes of the antenna be estimated?

The antenna noise efficiency derivation described in the next section and in Appendix A is based upon the plane-wave scattering-matrix (PWSM) theory of antennas [6]. This efficiency, because of reciprocity, reduces to the antenna radiation efficiency. However, in contrast to the usual definition [7] of the radiation efficiency, the PWSM description reveals enough of the structure of the efficiency to permit a detailed calculation and error analysis of its magnitude. The PWSM formalism is used solely to derive an expression for the antenna noise efficiency and excess noise temperature with the cavity in the antenna radiating near field, and to show how the efficiency can be evaluated in terms of antenna far-field quantities.

With the noise efficiency defined in Appendix A, insights gleaned from the Uniform Theory of Diffraction (UTD) [8] are used in Appendix B to eliminate its angle-dependent components. The error

incurred from neglecting these contributions to the efficiency is then estimated. The residual, angle-independent part of the efficiency is estimated in Appendix C by substituting the rectangular waveguide expression for the absorption coefficient, changing the cross-sectional dimensions to conform to the interior dimensions of the horn antenna. The waveguide expression is used because of the nonexistence of pyramidal horn mode equations. An estimate of the error caused by this substitution is also presented in Appendix C.

Effects of surface roughness on dissipative loss are reviewed in Appendix D where an attempt is made to clarify some disagreements found in the literature [9,10]. A modified expression for the corresponding noise efficiency is also presented.

Due to more intense fields in the waveguide portion of the horn, dissipative loss is greater there than in the horn flare. Consequently, the horn waveguide lead is made as short as possible without introducing a significant amount of higher-mode contamination in the antenna noise temperature. The minimum allowable length is determined in Appendix E along with an estimate of the error due to these higher modes.

The UTD is used in Appendix F to estimate the noise temperature error due to the cavity wall temperature being greater than the temperature of the absorber, and, in Appendix G, to estimate the effect of multiple reflections between the horn and rear cavity wall. Appendix F sets an upper limit to the magnitude of the excess cavity noise, while Appendix G justifies (by examining multiple reflections between the horn aperture and rear cavity wall) separating the total excess noise into a sum of excess antenna and cavity noises.

The design equations and construction details will be described in a companion document.

2. Antenna noise efficiency and construction of the horn

The antenna noise temperature T_n is determined from eq (1) with a different excess noise temperature ΔT than that given in eq (2) for transmission-line type noise standards. This new correction temperature has the form

$$\Delta T = (1 - \alpha)\ (T_o - T_m) \tag{3}$$

for an antenna inside a reflectionless, isothermal cavity. α is the noise efficiency defined in Appendix A, T_o is the physical temperature of the antenna, and T_m is the physical temperature of the cavity. An equation for the efficiency, when the cavity is in the radiating near field of the antenna, is derived by use of the antenna scattering matrix [6] and the Clausius statement of the second law of thermodynamics [11]. The details of the derivation given in the appendix reveal that the cavity walls need not be strictly reflectionless, only that no multiple reflections take place between the cavity and the antenna (an important distinction that is utilized in constructing the standard).

One interesting and useful feature that comes from the derivation is that the efficiency is the same whether the radiating sources (the cavity) are in the antenna near or far field. This result allows the efficiency to be more easily evaluated with far-field quantities.

$$\alpha = \frac{1}{\Omega_a} \int \left| \frac{r\underline{E}'(\underline{r})}{r\underline{E}(\underline{r})} \right|^2 P_n(\Omega) d\Omega \tag{4}$$

and is obtained by combining eqs (A19), (A26), and (A27) from the appendix--noting that the reflection coefficient of the antenna does not depend significantly ($S_{oo} = S'_{oo}$) on the antenna loss. In eq (4), Ω_a is the antenna solid angle, $\underline{r}$ is the radius vector from the antenna aperture to the far-field point (r is the magnitude), $P_n(\Omega)$ is the normalized power pattern where Ω stands for the antenna pointing angles, $d\Omega$ is the differential solid angle, and $r\underline{E}(\underline{r})$ is the E-field pattern. The prime refers to the real (lossy) antenna, the unprimed quantities belonging to the same antenna with no losses.

Ideally, the pattern ratio in eq (4) could be measured, or calculated from Maxwell's equations, but the measurement is too inaccurate to be useful and the calculation is prohibitively difficult. However, since most of the loss comes from the waveguide and flare portions of the horn (Appendix B), the efficiency is easily calculated (Appendix C) if losses from the remainder of the horn are neglected. Figure 2 shows an isometric view of the horn designed for the WR10 frequency band (75 GHz to 110 GHz) to take advantage of this situation. Reflections from the waveguide-flare junction, or throat, are minimized by joining the waveguide and flare with a circular arc of sufficiently large radius [12], beginning at x_1 and ending tangentially on the flared walls. A quarter-round (3 wavelength radius) matching section [13] at the aperture, in addition to a large aperture cross section [14], minimize the aperture reflections. With multiple reflections interior to the horn eliminated, a wave entering the horn flare from the waveguide maintains its TE_{10}-mode configuration out to the aperture.

Before including the throat taper and the aperture matching section into the design, and after choosing the E-plane aperture dimension, Braun's equations [15] were used to determine the other aperture dimension and the flare angles and lengths to insure approximately equal E- and H-plane beam widths and a simple butt joint at the waveguide-flare junction. The waveguide length x_1 was chosen (Appendix E) to minimize the effects of higher modes (generated by radiation incident on the antenna from the cavity) on the antenna noise temperature. Finally, a water jacket was included around the waveguide-throat region to maintain this high-loss area at a constant known temperature.

The horn attenuation calculated in Appendix C neglects the effect of surface roughness on the losses, predicting a loss that is less than the actual value. In Appendix D, it is argued that, for an isotropically rough surface, the horn attenuation coefficient increases by a factor K, which is independent of position inside the horn--depending only upon the roughness of the surface and the operating frequency. Furthermore, it is reasonable to assume that K is independent of temperature. These considerations imply that K can be determined by comparing the measured and calculated (assuming no surface roughness) attenuation for a waveguide section with the same surface roughness as the horn. A picture of the horn with the four waveguide sections and quarter-wave

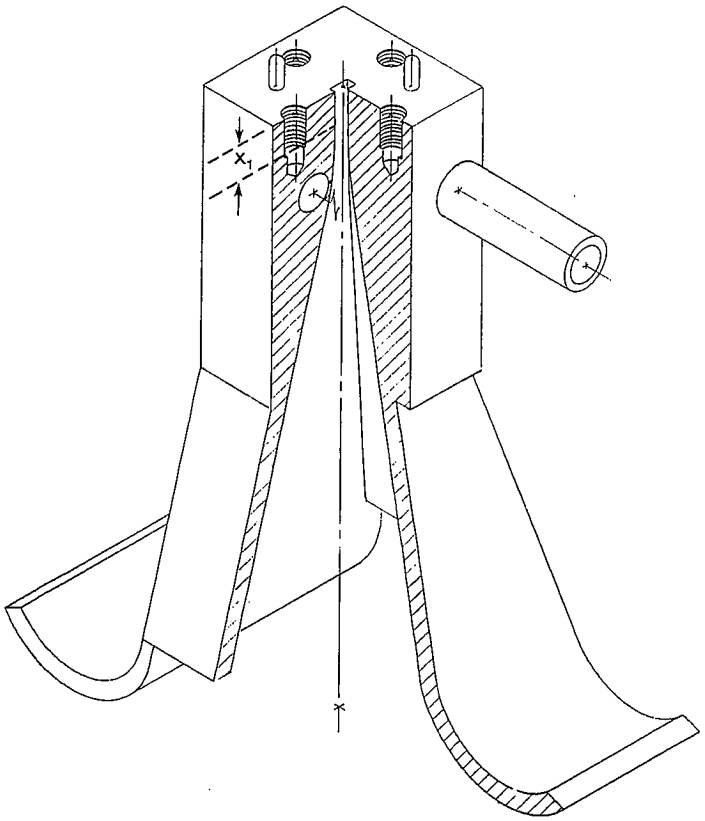

Figure 2. Isometric view of the WR10 horn antenna.

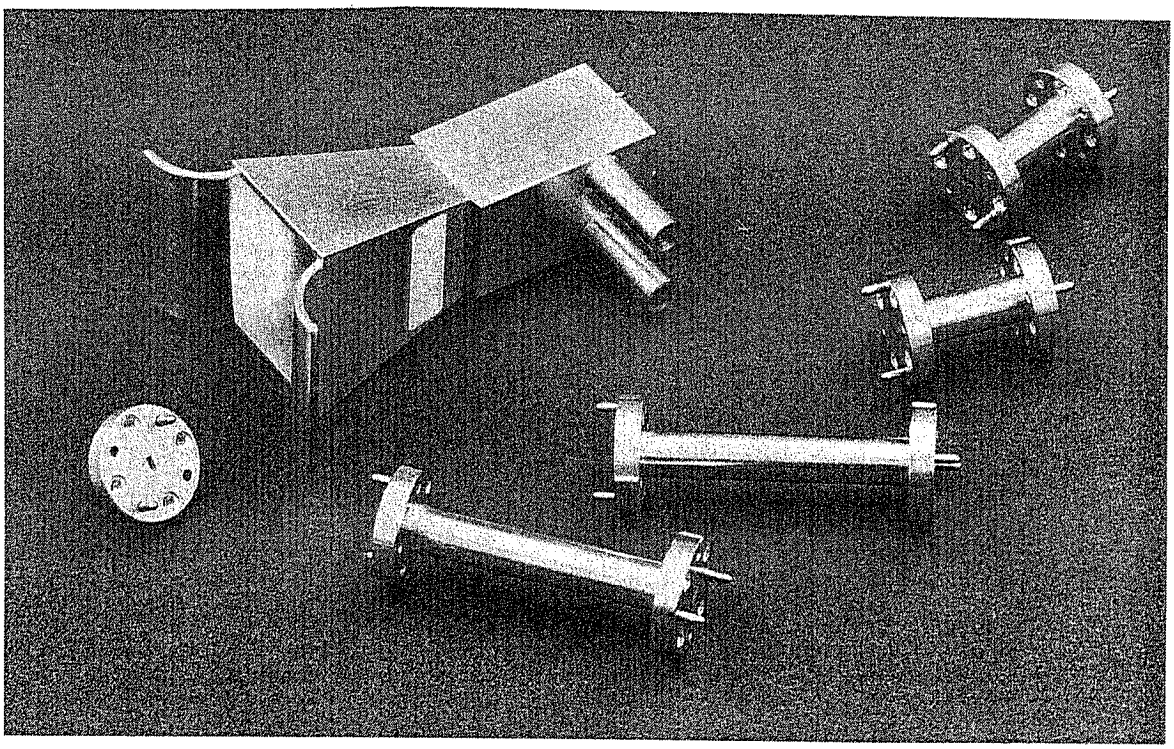

Figure 3. WR10 horn antenna, waveguide sections, and quarter-wave short.

short (94.5 GHz) used to determine K is shown in figure 3. The horn was constructed by machining a stainless-steel mandril to the interior horn dimensions, flashing it with gold, and electroforming copper on top of the gold. After electroforming and machining, the mandril was removed, leaving the horn shown in the figure. The process was repeated to produce the four waveguide sections with the same interior surface roughness as the horn. Then, after determining K for the waveguide section, the efficiency of the horn was calculated from

$$\alpha = e^{-2K\int a' dz} \tag{5}$$

where the attenuation coefficient a' (Appendix C) is a function of the dimensions and temperature of the horn at position z along the horn axis. The integral is performed over the length of the horn.

Figures 4, 5, and 6 show the results of the calculations with K = 1. The attenuation coefficient a' for 75 GHz and 110 GHz is plotted as a function of z along the horn axis, with the waveguide flange of the horn at the origin. The waveguide portion of the horn extends from z = 0 to

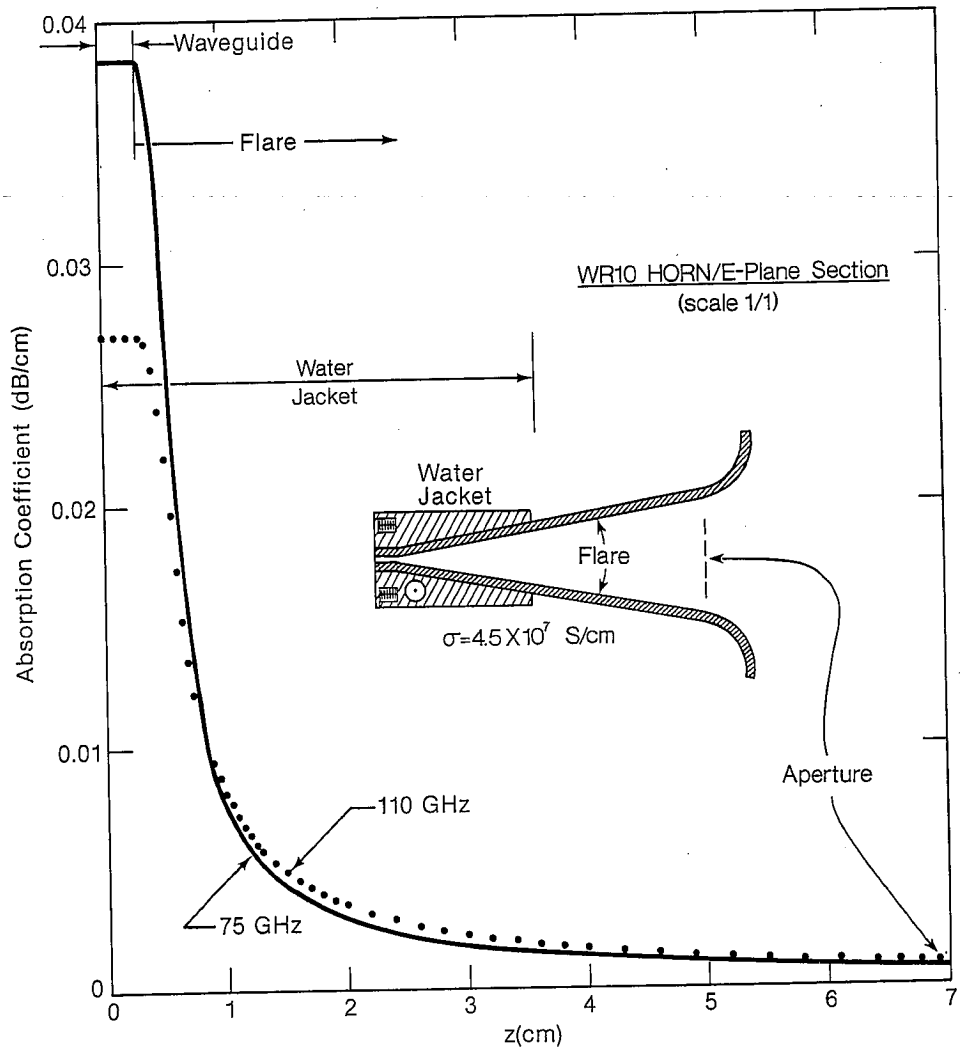

Figure 4. Attenuation coefficient for the WR10 horn antenna.

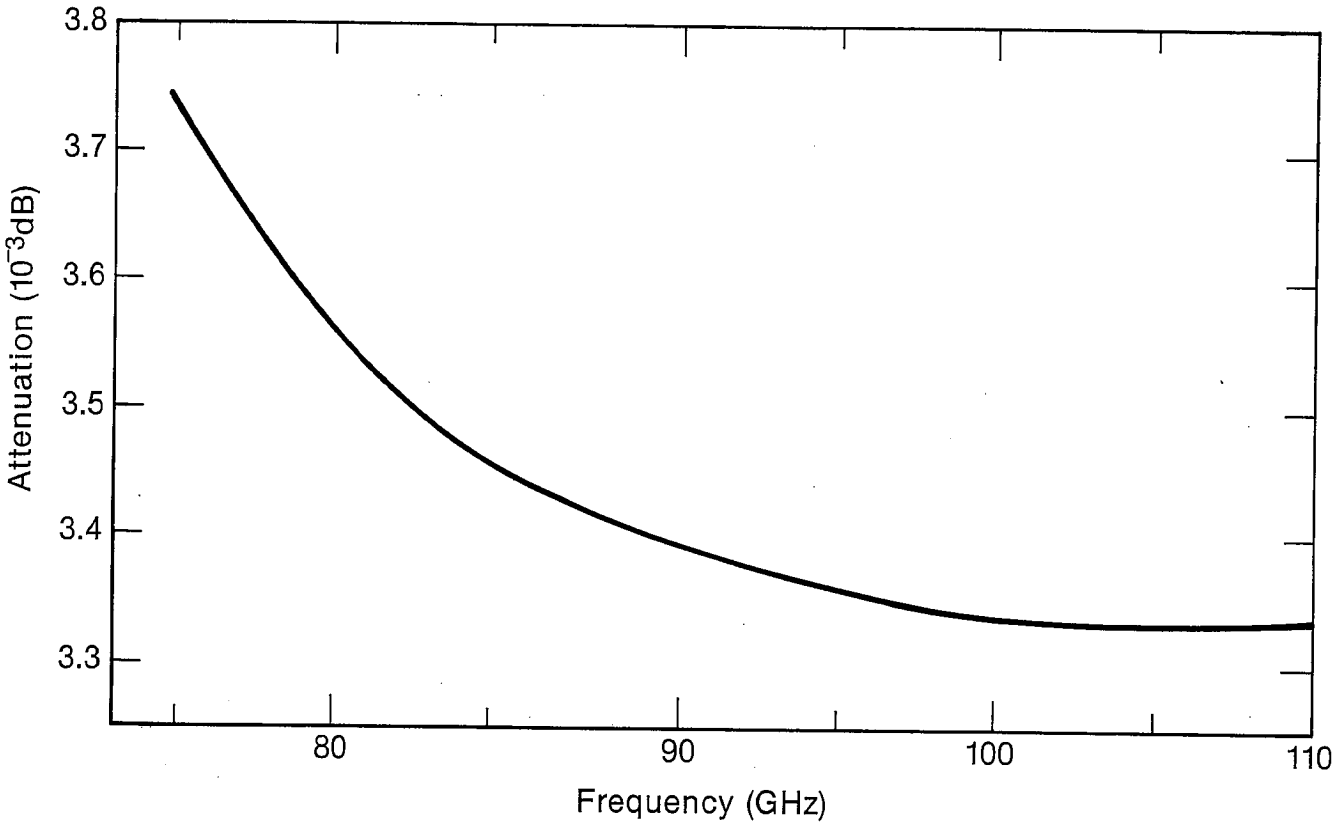

Figure 5. Attenuation versus frequency for the waveguide, throat, and flare portions of the WR10 horn antenna

z = 0.31, where the transition to the flare starts. The aperture and the beginning of the quarter-round matching sections are at z = 7.0, and the water jacket extends from the flange to z = 3.6. Figure 5 shows the total horn attenuation (the exponent of eq (5) with K = 1) as a function of frequency, leading to the excess noise temperature shown in figure 6.

3. Construction and operation of the cavity

An assembly drawing of the WR10 noise standard is shown in figure 7. The horn antenna is suspended at the top of the cavity by a yoke (items 18A and 18B) that attaches it to a flexible, beryllium-copper membrane (17) which fits loosely in a holder (7) that allows approximately 8 mm side motion. This motion, with the flexibility of the membrane, permits the horn waveguide flange to be connected to a radiometer without supporting the weight of the entire standard, greatly reducing problems associated with flange misalignment. The cavity consists of the yoke and membrane, the silicon-carbide absorber (13), and the load holder (14). The inside cavity walls are polished and gold flashed to reduce thermal radiation from their surfaces. Two radiation shields (6C, 6E) help reduce the amount of external radiation entering the cavity. The bottom portion of the cavity is immersed in liquid nitrogen, allowing the liquid to leak through the bottom of the holder and be absorbed by the silicon carbide. The liquid level is maintained between the maximum and minimum levels shown in the figure. Millimeter-wave absorber (16) is inserted between the bottom of the load holder and the vacuum flask (12) to absorb radiation entering the flask from outside the standard. By using this absorber, the radiation temperature [16] of the radiation entering the cavity from the flask area is reduced from approximately 300 K to 2 K above the boiling temperature (77 K) of the liquid. Once the flask is filled to the maximum level, it takes approximately seven

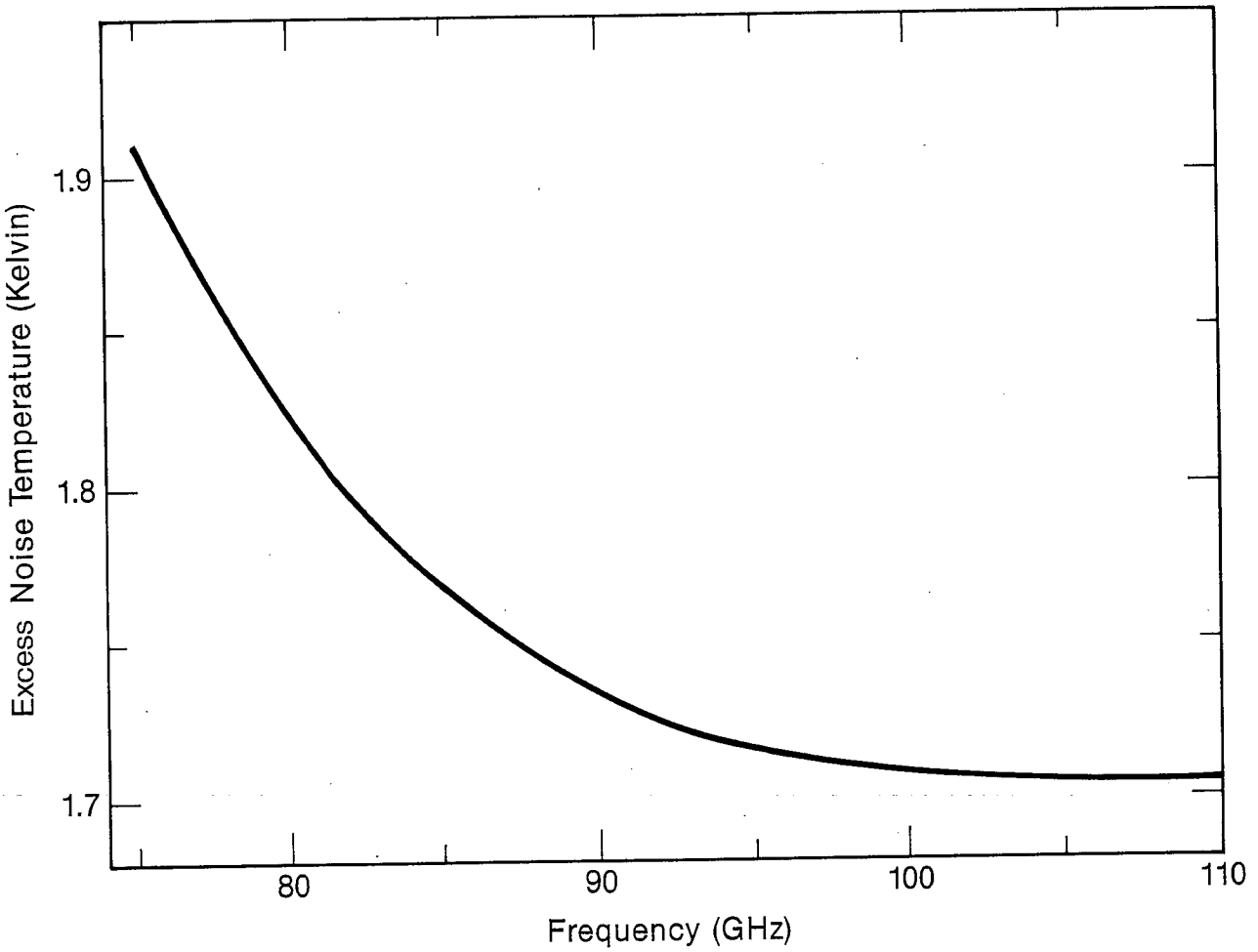

Figure 6. Correction noise temperature for the WR10 noise standard.

hours for the liquid to boil down to the minimum usable level. Figure 8 is a photograph of the completed assembly.

The silicon-carbide absorber was manufactured from commercially available grinding-wheel stock (grad P, grit C320, vitrified bond, silicon carbide) by cutting the stock into rectangular shapes and sharpening the ends. The pieces were then fastened together and the assembly ground to form the cylindrical shape shown in figure 9. When inserted in the holder (fig. 10), the cohesive action between the silicon-carbide particles and the liquid nitrogen draws the liquid up into the wedges, allowing the liquid to boil off on the wedge surfaces. With this technique, the temperature of the radiating surface of the absorber is maintained at the boil-off temperature of the liquid nitrogen to within 0.2 K, independent of the level of the liquid in the flask.

4. Results, errors, and conclusions

Equations (1), (3), and (5) are used to calculate the noise temperature T_n of the standard, where T_m is the measured temperature (liquid nitrogen boil-off temperature) of the absorber, T_o is the temperature of the horn antenna (room temperature), α is the noise efficiency of the horn, K is the roughness factor, and a' is the absorption coefficient at position z along the horn axis. Six

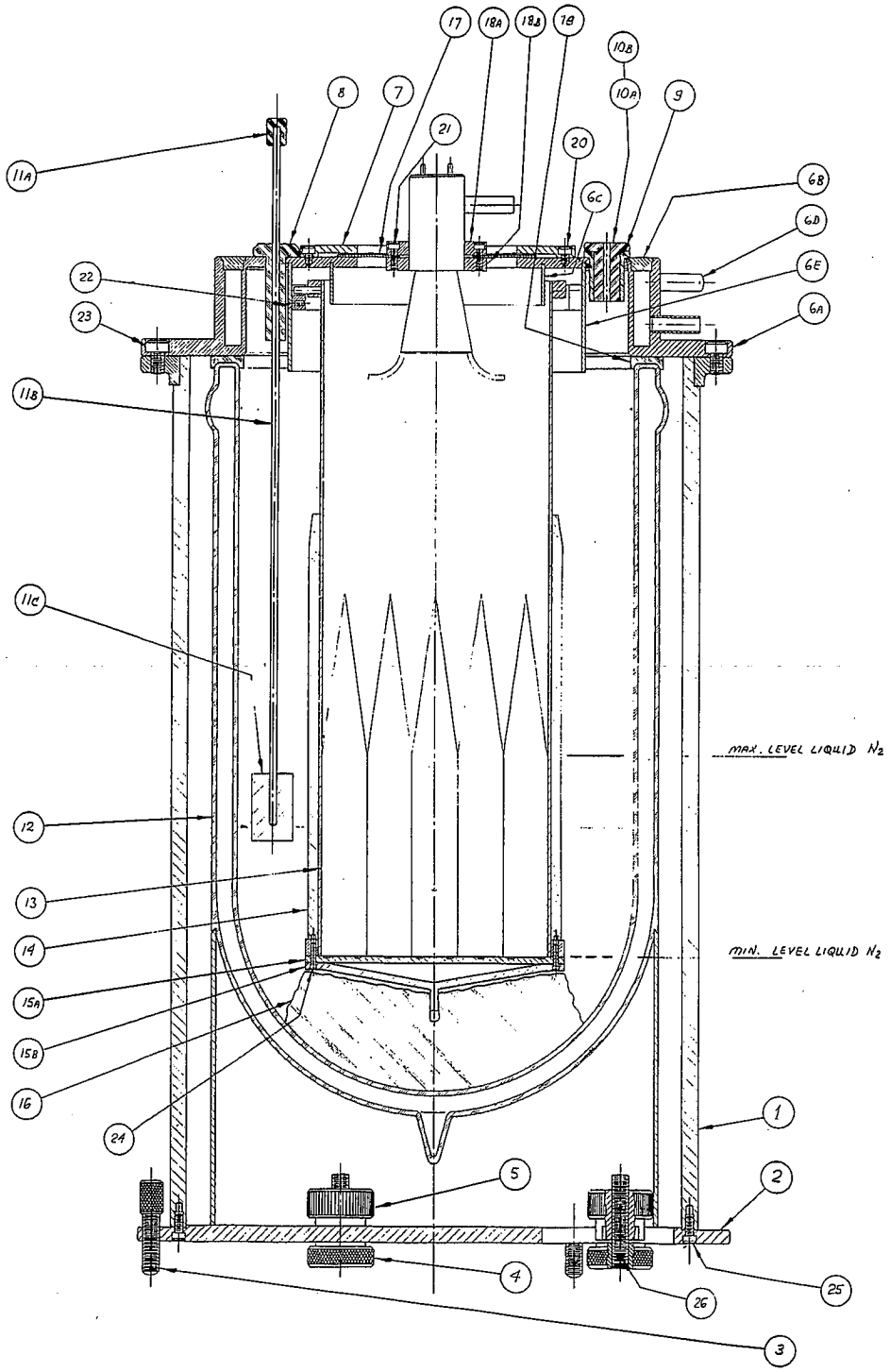

Figure 7. Assembly drawing of the WR10 noise standard.

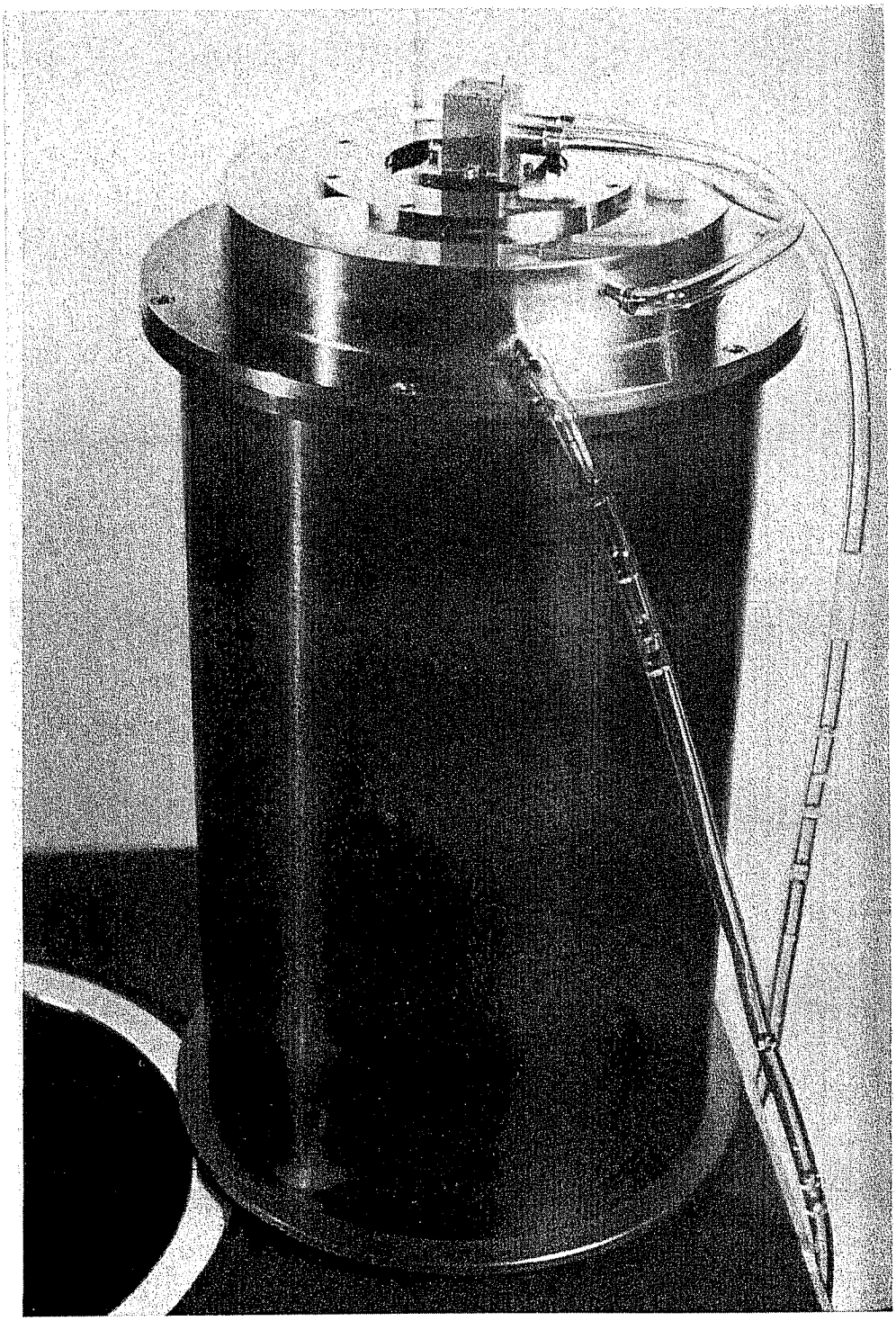

Figure 8. WR10 noise standard.

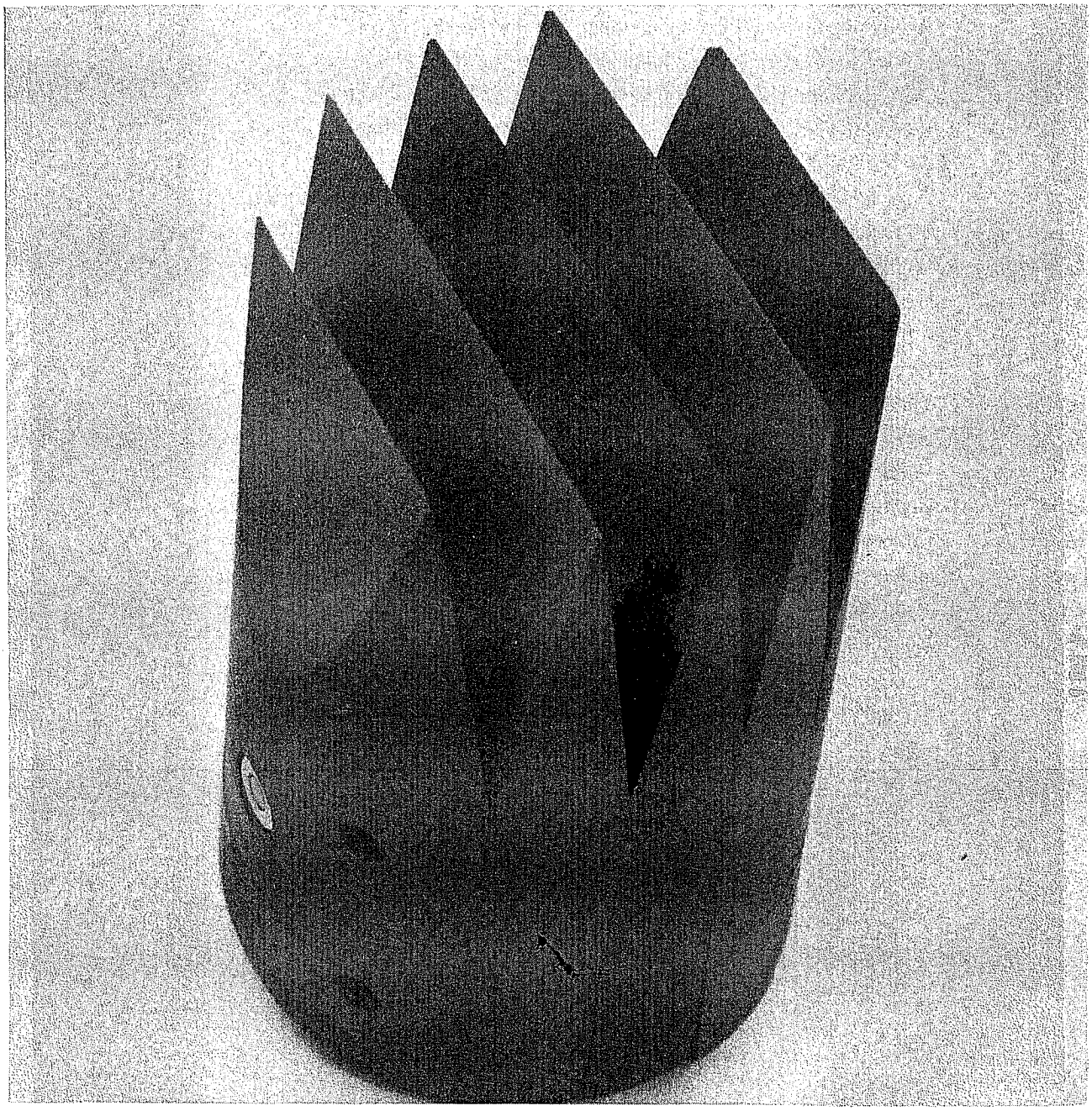

Figure 9. Silicon-carbide absorber.

possible sources of error accompany the use of these equations: (i) higher-mode contamination of the noise temperature, (ii) multiple reflections between the horn and rear cavity wall, (iii) wall temperatures greater than the absorber temperature, (iv) uncertainty in T_m, (v) uncertainty in T_o, and (vi) uncertainties in the noise efficiency. These sources of error are discussed below and summarized in table 1 along with the resulting errors they produce in the output noise temperature.

The length of the waveguide portion of the horn was chosen to adequately filter out the higher waveguide modes generated in the horn flare by radiation from the cavity incident on the horn. The calculations described in Appendix E show, that for 0.31 cm, the residual contamination amounts to no more than + 0.12% of the noise temperature.

Multiple reflections between the back wall of the cavity and the horn affect both the validity and magnitude of the correction noise temperature in eq (3). Calculations in Appendix G show the discrepancy in the magnitude to be insignificant, indicating that the assumption of a reflectionless cavity in the derivation of eq (3) leads to no larger an error than - 0.05%.

The temperature of the cavity back and side walls varies from room temperature at the top of the cavity (fig. 7) to liquid-nitrogen temperature where the side wall meets the absorber. The elevated wall temperatures cause the noise temperature to be in excess of the load temperature T_m. The resulting error (Appendix F) is no larger than - 0.10%.

The temperature of the absorber wedges was found to be within 0.1 K (the experimental error) of the liquid-nitrogen boil-off temperature (which was measured with the same thermocouple). When the standard is in use, the absorber temperature is determined by reading the atmospheric pressure (± 1 mm Hg) off a precision barometer and converting to the boil-off temperature (± 0.14 K) via standard vapor-pressure equations [17]. Care was taken in constructing the standard to insure a positive flux of nitrogen boil-off gas from the enclosure, preventing contamination of the liquid nitrogen by atmospheric gasses, and allowing the equations to be used to an assumed accuracy of 0.02 K. The total error (0.26 K) in measuring the absorber temperature is the sum of these three errors. This causes an error of less than 0.34% in the noise temperature.

Table 1. Errors in the WR10 (75 GHz - 110 GHz) noise standard

Source of Error	Source Uncertainty	Resulting Percentage Error in T_n
1. Higher modes	---	0
2. Multiple reflections between horn & cavity	---	+0 - 0.05
3. Elevated cavity-wall temperature	---	+0 - 0.10
4. Uncertainty in T_m	± 0.26 K	± 0.34
5. Uncertainty in T_o	± 2 K	± 0.02
6. Uncertainties in α		
6.1 Neglecting losses beyond aperture	---	+ 0 - 0.01
6.2 Using waveguide loss equation	---	± 0.01
6.3 Dimensional uncertainties	± 0.0025 cm	± 0.06
6.4 Uncertainties in dc resistivity curve	± 5%	± 0.01
6.5 Uncertainties in K	± 5%	± 0.06
Total error (linear sum)		+ 0.5 % - 0.7 %

The temperature of the horn, reduced slightly by cooling from the liquid-nitrogen boil-off gas, is determined by circulating room-temperature water through the water jacket (fig. 2). The water temperature is measured before entering the horn by use of a precision (± 1 K) mercury thermometer, and the temperature of the high-loss portions of the horn is depressed no more than 1 K by the boil-off gas. The horn temperature error is, therefore, no larger than 2 K, causing an error of less than 0.02% in the noise temperature.

Errors in the noise efficiency fall into two classes: errors due to the approximations leading to eq (5), and errors due to uncertainties in the parameters used in the equation. The first class contains an error due to neglecting dissipative horn losses beyond the aperture (Appendix B), resulting in a noise temperature error less than a negative 0.01%; and an error due to the nonexistence of equations describing pyramidal horn fields (Appendix C) resulting in an error no larger than 0.01%. The parametric errors are due to uncertainties (± 0.0025 cm) in the internal horn dimensions, in the slope versus temperature curve for the dc resistivity of the horn walls (± 5%), and in the roughness factor K. The first two result in noise-temperature errors of less than 0.01% and 0.06%, respectively.

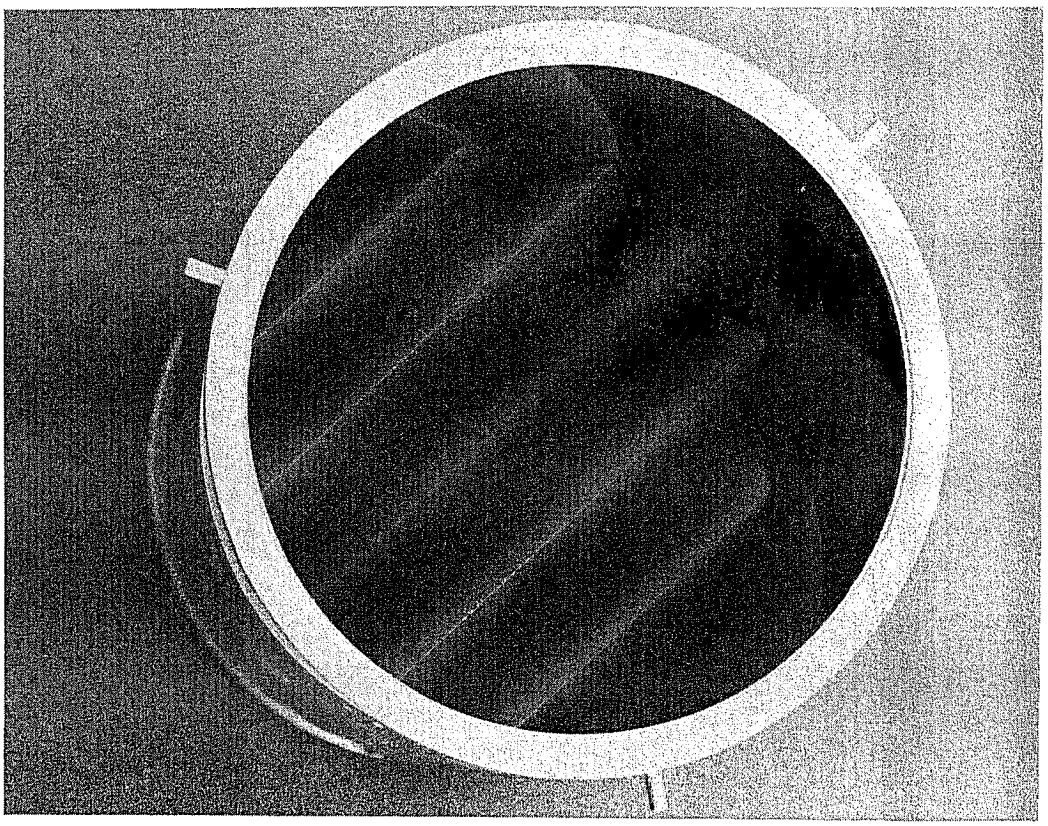

Figure 10. Top view of the cavity.

The roughness factor at 297 K was determined by comparing the measured and calculated values of attenuation for the waveguide sections shown in figure 3. Errors in the roughness factor are due to errors (± 0.0012 cm) in the measured dimensions of the waveguide sections, and uncertainties associated with the six-port millimeter-wave system [18] used to measure the attenuation. The roughness factor was determined to be 1.14 (± 0.05) at 94.5 GHz, with an error no larger than 0.06% in the noise temperature.

The sum of errors in table 1 for the noise-temperature output of the noise standard is within 1%, showing that it is possible to construct a precision horn/absorber type of standard, and, thus, eliminate the engineering problems mentioned in the introduction. Furthermore, this type of standard can be easily duplicated at the higher millimeter-wave bands.

Calculations using the UTD show that, if the yoke and membrane (items 17, 18A, and 18B in fig. 7) are removed from the standard, the noise temperature increases by approximately 0.7%. If, in addition, the aperture-matching quarter-rounds (the curved sections on the horn aperture in fig. 2) are removed from the horn, this figure increases from 0.7% to approximately 3%. Therefore, the yoke and membrane are needed to insure an accurately known noise temperature.

5. Acknowledgments

The author takes great pleasure in acknowledging the many beneficial contributions from his colleagues in the Electromagnetic Fields Division who unhesitatingly shared their expertise in a number of seminars and many private discussions.

6. References

[1] Arthur, M. G.; Driver, L. D. A precision HF-noise power measurement system. ISA Transactions, 10: 264 - 268; 1971.

[2] Wells, J. S.; Daywitt, W. C.; Miller, C. K. S. Measurement of effective temperature of microwave noise sources. IEEE Trans. on I&M, IM-13: 17 - 28; 1964 March.

[3] Daywitt, W. C. WR15 thermal noise standard. Nat. Bur. Stand. (U.S.) Tech. Note 615; 1972 March.

[4] Tischer, F. J. Experimental attenuation of rectangular waveguides at millimeter wavelengths. IEEE Trans. on MTT, MTT-27, No. 1: 31 - 37; 1979 January.

[5] Hansen, R. C. "Aperture Theory," Microwave Scanning Antennas, Vol. 1., New York, NY: Academic Press; 1964.

[6] Kerns, D. M. Plane-wave scattering-matrix theory of antennas and antenna-antenna interactions. Nat. Bur. Stand. (U.S.) Monogr. 162; 1981 June.

[7] IEEE standard definitions of terms for antennas. IEEE Std. 145-1973.

[8] The modern geometrical theory of diffraction. Vol. 1, Electro-Science Laboratory, The Ohio State University; 1982.

[9] Benson, F. A. Waveguide attenuation and its correlation with surface roughness. Proc. IEE, 100, Part III: 85 -90; 1953 March.

[10] Allison, J; Benson, F. A. Surface roughness and attenuation of precision-drawn, chemically polished, electropolished, electroplated and electroformed waveguides. Proc. IEE, 102B: 251 - 259; 1955 March.

[11] Allis, W. P.; Herlin, M. A. Thermodynamics and statistical mechanics. New York, NY: McGraw-Hill Book Company, Inc.; 1952.

[12] Terzuoli, A. J., Jr.; Peters, L., Jr. VSWR properties of E-plane dihedral corrugated horns. IEEE Trans. on A & P, AP-26, No. 2: 236 - 239; 1978 March.

[13] Burnside, W. D.; Chuang, C. W. An aperture-matched horn design. IEEE Trans. on A & P, AP-30, No. 4: 790 - 796; 1982 July.

[14] Jull, E. V. Reflection from the aperture of a long E-plane sectoral horn. IEEE Trans. on A & P, AP-20, No. 1: 62 - 68; 1972 January.

[15] Braun, E. H. Some data for the design of electromagnetic horns. IEEE Trans. on A & P, AP-4: 29 - 31; 1956 January.

[16] Ko, H. C. Antenna temperature and the temperature of electromagnetic radiation. IEEE Trans. on A & P, AP-12: 126 - 127; 1964 January.

[17] Jacobsen, R. T.; Stewart, R. B.; McCarty, R. D.; Hanley, H. J. M. Thermophysical properties of nitrogen from the fusion line to 3500 R (1944 K) for pressures to 150,000 PSIA (10343 x 10^5 N/m^2). Nat. Bur. Stand. (U.S.) Tech. Note 648; 1973 December.

[18] Weidman, M. WR-10 single six-port measurement system. Nat. Bur. Stand. (U.S.) NBSIR 81-1650; 1981 September.

[19] Yaghjian, A. D. Near-field antenna measurements on a cylindrical surface. Nat. Bur. Stand. (U.S.) Tech. Note 696; 1977 September.

[20] Morse, P. M.; Feshbach, H. F. Methods of theoretical physics, Part II. New York, NY: McGraw-Hill; 1953. p. 1764.

[21] Middleton, D. An introduction to statistical communication theory. New York, NY: McGraw-Hill Book Company, Inc.; 1960.

[22] Burkhard, D. G.; Lockhead, J. V. S.; Penchina, C. M. On the validity of Kirchhoff's law in a nonequilibrium environment. Amer. J. Phys., Vol. 40: 1794 - 1798; 1972 December. Baltes, H. P. On the validity of Kirchhoff's law of heat radiation for a body in a nonequilibirum environment. Progress in Optics, XIII, North-Holland: 3 - 25; 1976.

[23] Jull, E. V. Errors in the predicted gain of pyramidal horns. IEEE Trans. on A & P, AP-21: 25 - 31; 1973 January.

[24] Barrow, W. L.; Chu, L. J. Theory of the electromagnetic horn. Proc. IRE: 51 - 64; 1939 January.

[25] Lewin, L. Theory of waveguides. New York, NY: John Wiley & Sons; 1975.

[26] Karbowiak, A. E. Theory of imperfect waveguides: The effect of wall impedance. Proc. IEEE, 102, Part B: 698 - 708; 1955 September.

[27] Silver, S.; ed. Microwave antenna theory and design. Radiation Laboratory Series, Vol. 12, Boston Technical Publishers, Inc.; 1964.

[28] Bateman, H. Higher transcendental functions. Vol. II; New York, NY: McGraw-Hill Book Company, Inc.; 1953.

[29] Jackson, J. D. Classical electrodynamics. New York, NY: John Wiley & Sons, Inc.; 1962.

[30] Korn, G. A.; Korn, T. M. Mathematical handbook for scientists and engineers. New York, NY: McGraw-Hill Book Company, Inc.; 1968.

[31] Morgan, S. P. Effect of surface roughness on eddy current losses at microwave frequencies. J. Appl. Phys., 20: 352 - 362; 1949.

[32] Born, M.; Wolf, E. Principles of optics. New York, NY: Pergamon Press; 1959.

[33] Stratton, J. A. Electromagnetic theory. New York, NY: McGraw-Hill Book Company, Inc.; 1941.

[34] Siegel, R.; Howell, J. R. Thermal radiation heat transfer. New York, NY: McGraw-Hill Book Company, Inc.; 1981.

[35] Miller, C. K. S.; Daywitt, W. C.; Arthur, M. G. Noise standards, measurements, and receiver noise definitions. Proc. IEEE, Vol. 55, No. 6: 865 - 877; 1967 June.

Appendix A: The noise efficiency and noise temperature of an antenna in a reflectionless, isothermal cavity

The derivation for the antenna noise efficiency presented in this appendix employs the PWSM theory [6] of antennas, and consists of two steps. First, a spectral-density function for the cavity radiation is found by placing a lossless, reciprocal antenna in the cavity and applying thermodynamic arguments. The density function is then used with a lossy antenna in the cavity to find an expression for the resulting antenna noise efficiency and noise temperature. The PWSM theory and symbols are fully explained in the reference, and will not be reviewed here in order to save space.

Figure 11 and the use of plane-wave spectra to describe the cavity fields suggest that the results are applicable only to an infinite, parallel-plate cavity. However, the results are more general than indicated, and apply as well to a closed cavity, the PWSM formalism being used for convenience because of its extensive development in the antenna metrology area. A rigorous derivation for the closed cavity would proceed along the lines of Yaghijian's cylindrical surface

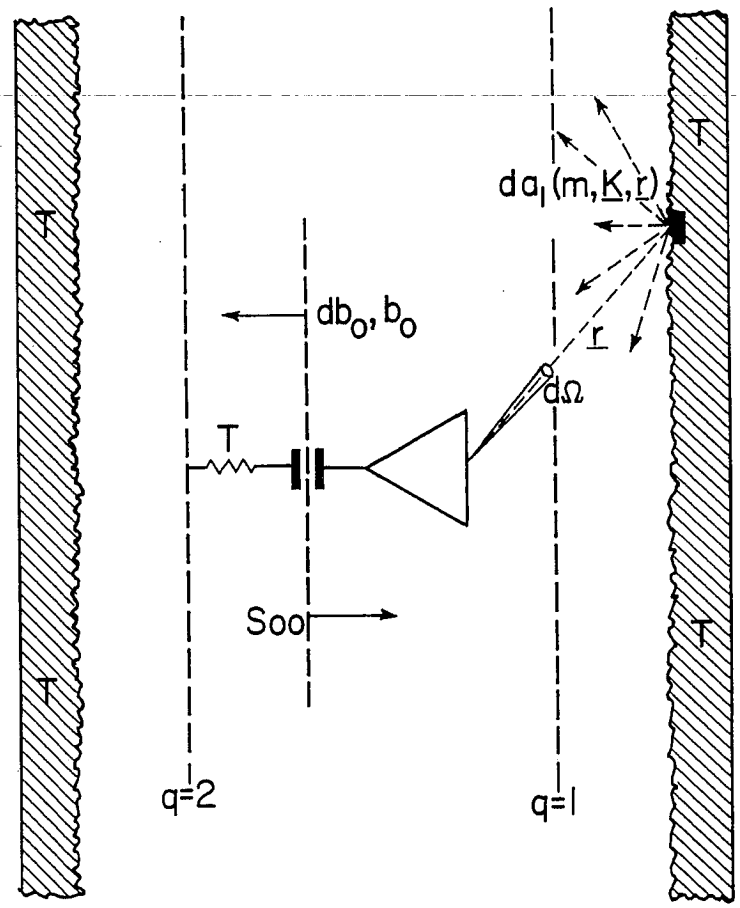

Figure 11. Schematic diagram of an antenna and termination in a reflectionless, isothermal cavity.

formulation [19] except for the use of spherical-wave expansions which [20], like their cylindrical-wave counterparts, allow a scattering-matrix description of the antenna to be developed that contains important orthogonality properties permitting a development similar to the one presented here to be accomplished.

Cavity radiation density function

Figure 11 shows a lossless antenna (terminated by a reflectionless load) in thermal equilibrium (via radiation through the antenna) with the cavity, leaving the load and cavity at the same temperature T. Here da_q (m, $\underline{K}$, $\underline{r}$) is a differential amplitude function for the radiation originating at position $\underline{r}$, where q (= ± 1) denotes the front and back hemisphere surrounding the antenna; m is the polarization index of the corresponding wave incident on the antenna; and $\underline{K}$ is the transverse (to the z-direction) part of the propagation vector $\underline{k}$. The wave amplitude of the field in the antenna waveguide lead produced by da_q is represented by db_o, whose summation over both hemispheres is denoted by b_o. S_{oo} is the antenna reflection coefficient. Since there are no multiple reflections between the antenna and the cavity walls [6]

$$db_o = \not\sum S_{oq}(m, \underline{K})\, da_q(m, \underline{K}, \underline{r})\, \underline{dK} \tag{A1}$$

where

$$\not\sum \equiv \sum_q \int_{\underline{K}} \sum_m \tag{A2}$$

is a symbol used for convenience, and the integral is two dimensional, being performed over the product $dk_x\, dk_y$ symbolized by $\underline{dK}$. The integral limits are restricted to the region in $\underline{k}$-space where $K < k$, implying that there is no evanescent-mode coupling between the antenna and cavity. S_{oq} is the receiving characteristic of the antenna. The total wave amplitude is

$$b_o = \int_{4\pi} db_o = \not\sum S_{oq}(m, \underline{K}) \int_{4\pi} da_q(m, \underline{K}, \underline{r})\, \underline{dK} \tag{A3}$$

where the integral is over both hemispheres or 4π steradians.

The spectral density ω_o of the available power [21] corresponding to b_o is

$$\omega_o = \frac{\eta_o}{1 - |S_{oo}|^2} \langle b_o\, b_o^* \rangle \tag{A4}$$

where the bracket symbolizes an ensemble average, accounting for the fact that b_o is a stochastic variable [21], and where the asterisk stands for the complex conjugate. η_o is the characteristic admittance for the mode propagating in the waveguide. Combining eqs (A3) and (A4) leads to

$$\omega_o = \frac{\eta_o}{1 - |S_{oo}|^2} \not\sum \not\sum' S_{oq}(m, \underline{K})\, S^*_{oq'}(m', \underline{K}')\, \omega_c\, \underline{dK}\, \underline{dK}' \tag{A5}$$

where

$$\omega_c \equiv \int_{4\pi}\int_{4\pi} \langle da_q(m, \underline{K}, \underline{r})\, da^*_{q'}(m', \underline{K}', \underline{r}')\rangle \ . \tag{A6}$$

The power spectral density ω of the load attached to the antenna is

$$\omega = \kappa T \tag{A7}$$

where κ is Boltzmann's constant, and T is the load temperature. Since the load and cavity are in thermal equilibrium, the second law of thermodynamics [11] implies that

$$\omega_o = \omega \ . \tag{A8}$$

Combining eqs (A5), (A7), and (A8) leads to

$$\frac{\eta_o}{1 - |S_{oo}|^2} \oint\oint' S_{oq}(m, \underline{K})\, S^*_{oq'}(m', \underline{K}')\, \omega_c\, \underline{dK}\, \underline{dK}' = \kappa T \ . \tag{A9}$$

Since the antenna is lossless and reciprocal [6]

$$\frac{\eta_o}{1 - |S_{oo}|^2} \oint \frac{|S_{oq}(m, \underline{K})|^2}{\eta_m(K)}\, \underline{dK} = 1 \tag{A10}$$

where $\eta_m(K)$ is the wave admittance for the incident wave with polarization index m and transverse wave number K. The last equation can be rewritten in the form

$$\frac{\eta_o}{1 - |S_{oo}|^2} \oint\oint' \frac{S_{oq}(m, \underline{K})\, S^*_{oq'}(m', \underline{K}')}{\eta_m(K)}\, \delta_{qq'}\, \delta_{mm'}\, \delta(\underline{K}-\underline{K}')\, \underline{dK}\, \underline{dK}' = 1 \tag{A11}$$

where $\delta_{qq'}$ and $\delta_{mm'}$ are Kronecker delta functions, and $\delta(\underline{K}-\underline{K}')$ is a Dirac delta function. Multiplying eq (A11) by κT and combining it with eq (A9) leads to

$$\frac{\eta_o}{1 - |S_{oo}|^2} \Sigma\, \Sigma' S_{oq}(m, \underline{K})\, S^*_{oq'}(m', \underline{K}') \cdot \left[\omega_c - \frac{\kappa T}{\eta_m(K)}\, \delta_{qq'}\, \delta_{mm'}\, \delta(\underline{K}-\underline{K}')\right] \underline{dK}\, \underline{dK}' = 0 \ . \tag{A12}$$

The quantity in the brackets of this expression is a property of the cavity and independent of the antenna structure. Therefore, since eq (A12) must hold for any lossless, reciprocal antenna, the quantity in the bracket must vanish. This yields the required spectral function for the cavity radiation,

$$\omega_c = \frac{\kappa T}{\eta_m(K)} \delta_{qq'} \delta_{mm'} \delta(\underline{K}-\underline{K}') \ . \qquad \text{(A13)}$$

This function will be used in the next step to derive an expression for the noise efficiency of a lossy antenna in equilibrium with the cavity and termination.

Antenna noise efficiency and noise temperature

The antenna noise temperature T_n of a lossy antenna in the cavity is equal to the power spectral density (divided by Boltzmann's constant) of the total available noise powers at the antenna waveguide flange. The total power is the sum of the noise powers generated by the cavity and the dissipative losses in the antenna. Hence, the spectral density is the sum of the separate spectral densities of the antenna and cavity. The spectral density ω_1 for the cavity radiation appearing at the waveguide flange of the antenna can be obtained by inserting eq (A13) into eq (A5) and taking the cavity temperature T (since it is constant) out from under the integral sign. The result is

$$\omega_1 = \kappa T \alpha \qquad \text{(A14)}$$

where

$$\alpha \equiv \frac{\eta_o}{1 - |S'_{oo}|^2} \oint \frac{|S'_{oq}(m, \underline{K})|^2}{\eta_m(K)} \underline{dK}$$

$$= \frac{\eta_o \, k}{(1 - |S'_{oo}|^2) \, Y_o} \oint \frac{|\underline{s}'_{oq}(\underline{K})|^2}{Y} \underline{dK} \ . \qquad \text{(A15)}$$

The second sum-integral symbol includes only the sum over q since the sum over m is absorbed into the "complete" antenna receiving characteristic $\underline{s}'_{oq}$ [6]. Y_o is the wave admittance of free space, and the primes in the equation signify that the corresponding parameters belong to a lossy antenna. Note that, because of the loss, eq (A15) does not reduce to unity, as does eq (A10) for a lossless antenna. Equation (A15) defines the antenna noise efficiency. For a reciprocal antenna, it is equivalent to the antenna radiation efficiency [6].

The spectral density ω of the total available power at the waveguide flange is

$$\omega = \omega_1 + \omega_2 \qquad \text{(A16)}$$

where ω_2 is the spectral density for the antenna losses. Since the load terminating the antenna, the antenna itself, and the cavity are at the same temperature, the second law of thermodynamics implies that the ω of eq (A16) is the same as that of eq (A7). Therefore, eqs (A7), (A14), and (A16) can be solved for ω_2, yielding

$$\omega_2 = \kappa T(1 - \alpha) \ . \tag{A17}$$

This important result is used to calculate the amount of noise power generated by the antenna losses, and appearing at the antenna waveguide flange. When the temperature T_o of the antenna and the temperature T_m of the cavity are different, eqs (A14), (A16), and (A17) combine to give the antenna noise temperature T_n, where

$$T_n \equiv \kappa^{-1} \omega = T_m \alpha + T_o(1 - \alpha) \ . \tag{A18}$$

This result depends on the validity of Kirchhoff's law of radiation [22] in nonequilibrium ($T_m \neq T_o$).

It is useful to rearrange eq (A15) to the form

$$\alpha = \oint \eta_{oq}(\underline{K}) \, d\alpha \tag{A19}$$

where

$$\eta_{oq}(\underline{K}) \equiv \frac{1 - |S_{oo}|^2}{1 - |S'_{oo}|^2} \left| \frac{\underline{s}'_{oq}(\underline{K})}{\underline{s}_{oq}(\underline{K})} \right|^2 \tag{A20}$$

$$d\alpha \equiv \frac{\eta_o \, k \, |\underline{s}_{oq}(\underline{K})|^2}{Y_o \, \gamma(1 - |S_{oo}|^2)} \, \underline{dK} \tag{A21}$$

and γ is the z-component of the propagation vector. The antenna loss is now contained entirely in definition (A20) with the result that

$$\oint d\alpha = 1 \tag{A22}$$

which is equivalent to eq (A10). Since the antenna is reciprocal [6]

$$\eta_o \, k \, \underline{s}_{oq}(\underline{K}) = Y_o \, \gamma \, \underline{s}_{qo}(-\underline{K}) \tag{A23}$$

with a similar equation for the lossy or primed quantities. $\underline{s}_{qo}$ is the "complete" transmitting characteristic of the antenna. Equations (A20) and (A21) can now be expressed in terms of the transmitting characteristic

$$\eta_{oq}(\underline{K}) = \frac{1 - |S_{oo}|^2}{1 - |S'_{oo}|^2} \left| \frac{\gamma \, \underline{s}'_{qo}(-\underline{K})}{\gamma \, \underline{s}_{qo}(-\underline{K})} \right|^2 \tag{A24}$$

and

$$d\alpha = \frac{Y_o |\gamma \, \underline{s}_{qo}(-\underline{K})|^2}{\eta_o(1 - |S_{oo}|^2)} \frac{\underline{dK}}{k\gamma} \ . \tag{A25}$$

Equations (A24) and (A25) depend only upon the antenna structure, and apply when the noise sources in the cavity walls are in either the radiating near field [5] or the far field of the antenna. They may be conveniently evaluated in terms of the transmitted far field of the antenna [6] by using

$$\eta_{oq}(\underline{K}) = \frac{1 - |S_{oo}|^2}{1 - |S'_{oo}|^2} \left| \frac{r\underline{E}'_q(\underline{r})}{r\underline{E}_q(\underline{r})} \right|^2 \tag{A26}$$

and

$$d\alpha = \frac{P_n(q, \underline{K})\, d\Omega}{\Omega_a} \tag{A27}$$

where $r\underline{E}_q$ is the far field pattern, and P_n and Ω_a are the normalized power pattern and antenna solid angle, respectively. $d\Omega$ is the differential solid angle referenced to the antenna aperture. Combining eqs (A19), (A26), and (A27), and writing the integral in more conventional form,

$$\alpha = \frac{1 - |S_{oo}|^2}{1 - |S'_{oo}|^2} \cdot \frac{1}{\Omega_a} \int \left| \frac{r\underline{E}'(\underline{r})}{r\underline{E}(\underline{r})} \right|^2 P_n(\theta, \phi)\, d\Omega \tag{A28}$$

where θ and ϕ are the usual antenna angles, and where S_{oo}' and the field pattern $r\underline{E}'(\underline{r})$ contain the antenna loss. The integral is over the entire 4π solid angle. The ratio in the integrand is the ratio of the field pattern with loss to the field pattern without loss.

For convenience, the preceding development was done in the low-frequency approximation to the radiation laws. This approximation results in a 3% error in the present situation, and, therefore, the Planck quantum effects must be taken into account. This is done by replacing the low-frequency radiation temperatures appearing in the equations by their Planck equivalents. For example, T_m is replaced by the expression

$$\frac{h\nu/K}{e^{h\nu/kT_m} - 1} \tag{A29}$$

where h is Planck's constant, ν is the operating frequency, and K is Boltzmann's constant.

Appendix B: A simplified expression for the noise efficiency

For most horns, the first ratio in eq (A28) containing the reflection coefficient is not significantly different from unity and can be discarded. The noise efficiency becomes

$$\alpha = \frac{1}{\Omega_a} \int \left| \frac{\underline{rE}'(\underline{r})}{\underline{rE}(\underline{r})} \right|^2 P_n d\Omega \ . \qquad (B1)$$

The horn in figure 2 was designed to minimize throat and aperture reflections so that a transmitted signal consists of a simple traveling wave that maintains the TE_{10} spatial configuration of the waveguide mode as it travels from the waveguide flange to the aperture. The expansion and radiation of such a wave in the E plane of the horn is shown in figure 12. As the wave travels away from the flange, it behaves like a TE_{10} mode until it arrives at the aperture A-A'. Considering the θ-direction, the principle wavefront continues to travel outward [8] along ray S. Two diffracted waves [13] are set up at A and A' due to the abrupt change in curvature, portions of which travel out along rays D_1 and D_1'. Surface waves that are launched at A and A' travel along their respective quarter-rounds until they encounter the edges at B and B'. Again, diffracted waves are set up with

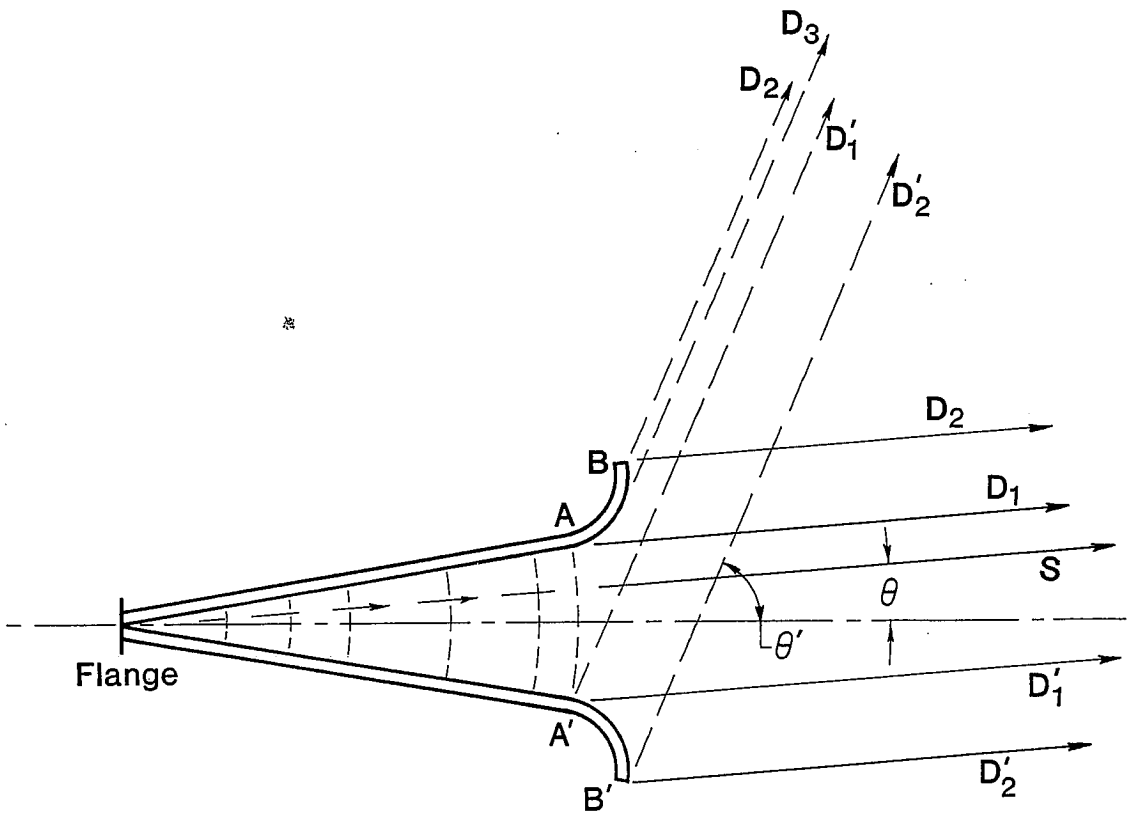

Figure 12. E-plane section of the WR10 horn antenna showing the traveling-wave field.

components traveling along rays D_2 and D_2' in the θ-direction. To first order, the process stops here. A similar explanation applies to the θ'-direction, except there the principle ray S is missing and a diffracted ray D_3 representing leakage from the surface ray is added. To the approximation considered, the field $\underline{E}'(\underline{r})$ in the θ-direction is the sum of the waves associated with the rays S, D_1, D_1', D_2, and D_2'. In the θ'-direction, the sum includes the rays D_1', D_2, D_2', and D_3. The components of the field attenuation at $\underline{r}$ can be seen from this decomposition: attenuation of the S, D_1 and D_1' waves is a result of the "waveguide" attenuation [23] η from the flange to the aperture; while in addition to this attenuation, the D_2 and D_2' waves suffer a further attenuation associated with the surface waves on the quarter-rounds. A similar interpretation applies to the θ'-direction, from which it is clear that the difference in the ratio of eq (B1) for the two directions θ and θ' is due to a difference in the wave attenuations beyond the aperture A-A'. Therefore, if the attenuation beyond A-A' is neglected by setting the ratio equal to η, then eq (B1) reduces to

$$\alpha = \eta \tag{B2}$$

since η is independent of the antenna angles and can be taken outside the integral and the integral without the ratio is the antenna solid angle.

The relative error in the antenna noise temperature due to neglecting the attenuation beyond A-A' can be obtained by combining eqs (A18), (B1), and (B2), resulting in

$$\frac{\Delta T_n}{T_n} = \left(\frac{T_o - T_m}{T_m}\right) \eta \int \left(1 - \Delta\eta(\theta, \phi)\right) \frac{P_n \, d\Omega}{\Omega_a} \tag{B3}$$

where $\Delta\eta$ denotes the efficiency associated with the additional attenuation and is equal to the ratio in eq (B1) divided by η. An upper bound is easily obtained by replacing $\Delta\eta$ in eq (B3) by its minimum value (corresponding to a maximum value of attenuation), reducing (B3) to

$$\frac{\Delta T_n}{T_n} = \left(\frac{T_o - T_m}{T_m}\right) \eta(1 - \Delta\eta) \, . \tag{B4}$$

For a conductivity of 4.5 S/cm (gold at room temperature), the minimum value of $\Delta\eta$ is estimated to be no less than 0.99965. Then, using T_o = 300 K, T_m = 77 K, and η = 1 leads to a maximum error of 0.10% in the noise temperature.

Appendix C: Evaluation of η

Precise evaluation of the antenna noise efficiency given by eq (B2) is not possible for a pyramidal horn because mathematical expressions for the fields inside the horn do not exist. In sectoral horns where expressions do exist, the electric and magnetic fields do not propagate with the same phase constant [24]. Even higher modes (other than TE_{mo} and TM_{mo}) in a lossy, overmoded, rectangular waveguide are not stable (i.e., retain the same field pattern along the guide) [25,26]. Nevertheless, the attenuation of the wave described in Appendix B will be calculated as though it were the dominant waveguide mode in a waveguide of slowly increasing transverse dimensions [23]. The error in using the dominant waveguide mode, instead of the nonexistent horn modes, is assumed to be the difference in the attenuation calculated this way and calculated by using the dominant mode fields for the E- and H-plane sectoral horns.

The attenuation coefficient a' for the fields is calculated from the expression [24]

$$a' \equiv \frac{1}{2P}\frac{dP}{dz} \tag{C1}$$

where P is the power traveling longitudinally through the waveguide (or radially through the sectoral horn with z = r), and dP/dz is the corresponding power loss per unit length due to dissipative wall losses.

$$P = \frac{1}{2}\,\mathrm{Re}\iint E \times H^* \cdot ds \tag{C2}$$

and

$$\frac{dP}{dz} = \frac{1}{2} R_s \int |H_t|^2 \, d\tau \ . \tag{C3}$$

H_t is the magnetic field tangent to the wall, τ is a transverse coordinate along the wall, and Re stands for the real part of the complex quantity of the arguement. The surface resistance R_s of the wall is related to the wave number k, skin depth δ, and free-space impedance Z_o by

$$R_s = \frac{1}{2} k \delta Z_o \ . \tag{C4}$$

The attenuation coefficient a'_w for the waveguide mode is easily found in the literature [25] as

$$a'_w = \frac{R_s}{\omega\mu\beta_g}\left(\frac{k^2}{b} + \frac{2k_c^2}{a}\right) \tag{C5}$$

where a and b are the cross-sectional dimensions of the waveguide, k_c (= π/a) is the cutoff wavenumber, ω is the radian frequency, μ is the magnetic permeability of the walls, and

$$\beta_g^2 = k^2 - k_c^2 \ . \tag{C6}$$

When the H-plane horn mode equations [27] are inserted into eq (C1), the resulting attenuation coefficient a'_H for the geometry shown in figure 13 is (the H's in the following equation are Hankel functions, and $p \equiv \pi/2\theta_H$)

$$a'_H = \frac{R_s}{\omega\mu\beta_g}\left\{\frac{1}{b}\left[k_c^2\left(\frac{a}{2r\theta_H}\right)\frac{|H_p^{(2)}(kr)|^2}{4\,\theta_H/\pi a\beta_g} + \beta_g^2\left(\frac{2r\theta_H}{a}\right)\frac{|H_p^{(2)'}|^2}{4\,\theta_H\,\beta_g/\pi ak^2}\right]\right.$$

$$\left. + \frac{2k_c^2}{a}\left(\frac{a}{2r\theta_H}\right)^2\frac{|H_p^{(2)}|^2}{4\,\theta_H/\pi a\beta_g}\right\} . \quad (C7)$$

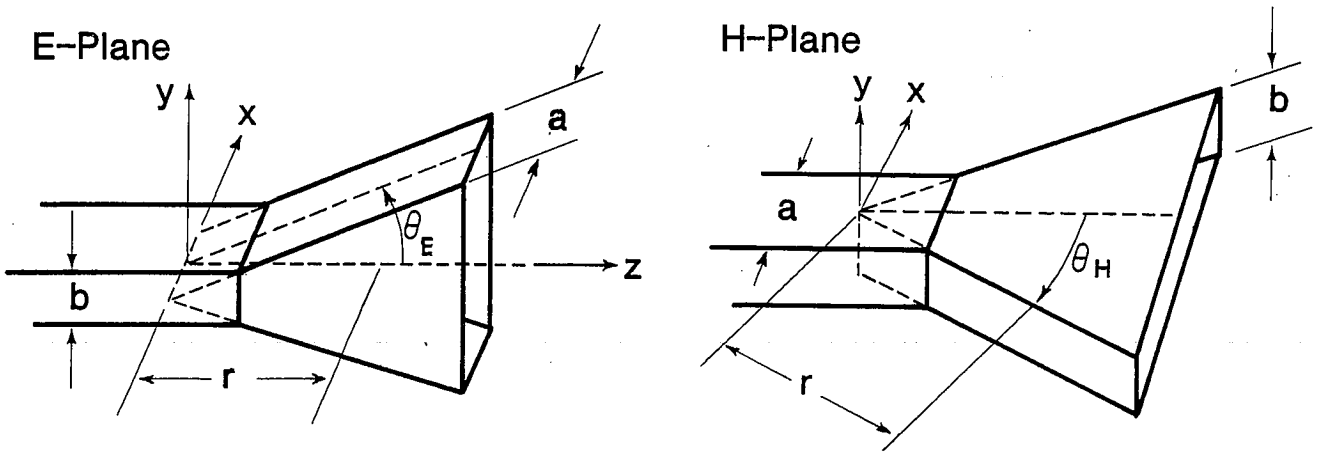

Figure 13. Diagram of an E-plane and a H-plane sectoral horn.

For the E-plane horn (fig. 13)

$$a'_E = \frac{R_s}{\omega\mu\beta_g}\left\{\frac{k^2}{b}\left(\frac{b}{2r\theta_E}\right)\left[\frac{|H_o^{(2)}(\beta_g r)|^2}{2/\pi r\beta_g} + \left(\frac{k_c}{k}\right)^2\frac{(|H_1^{(2)}|^2 - |H_o^{(2)}|^2)}{2/\pi\beta_g r}\right]\right.$$

$$\left. + \frac{2k_c^2}{a}\frac{|H_1^{(2)}|^2}{2/\pi\beta_g r}\right\} . \quad (C8)$$

Using the proper asymptotic expansions of the Hankel functions [28], both eqs (C7) and (C8) can be reduced to eq (C5) as the flare angles θ_H and θ_E vanish.

Equations (C5), (C7), and (C8) were used to calculate the attenuation and noise efficiency of the horn in figure 2 by varying the a and b dimensions to conform to the inner horn dimensions. The efficiency and attenuation A are related by the equations

$$\eta = e^{-A} \tag{C9}$$

$$A \equiv 2 \int a' dz \ . \tag{C10}$$

The integral in eq (C10) is performed over the length of the horn. The error due to substituting the waveguide mode fields for the nonexistant pyramidal horn mode equations was then assumed to be no greater (see eqs (A18) and (B2)) than

$$\frac{\Delta T_n}{T_n} = \left(\frac{T_o - T_m}{T_m}\right) (2\eta_W - \eta_H - \eta_E) \tag{C11}$$

where η_W, η_H, η_E are the efficiencies calculated by using the attenuation coefficients in eqs (C5), (C7), and (C8), respectively. This error was no larger than 0.01% for the entire WR10 frequency band (75 GHz - 110 GHz).

Appendix D: Surface roughness

The derivation outlined in this appendix was developed to help resolve a disagreement in the literature [9,10] concerning the proper form of the equation describing the effect of surface roughness on attenuation, and to extend these previous results into the range where the skin depth is comparable to the rms surface roughness.

Figure 14 illustrates the E field of an electromagnetic wave that is constrained to move along the z-direction of a rough, metallic surface where $\underline{n}$ is the unit normal to the surface, and ξ is the coordinate directed into the surface. $\underline{H_t}$ is the magnetic field tangent to the surface, and d^2P is a second-order differential representing the time-averaged Poynting vector directed into the surface as a result of the surface losses. By neglecting the displacement current in the metal and using Ampere's law [29] in the Poynting vector to eliminate electric field, the power absorbed by dA can be put in the form

$$\frac{d^2P}{dA} = \frac{R_s\delta}{2} \text{Re}\left[\underline{H_t^*} \cdot \left(-\frac{\partial \underline{H_t}}{\partial \xi}\right)\right] \tag{D1}$$

where R_s is the surface resistance, and δ is the skin depth.

Figure 15 shows a portion of the rough surface parallel to the x-z plane with surface coordinates [30]μ and υ. The small (but nonvanishing) surface area ΔA is bounded by the z and z + Δz planes, and the x and x + Δx planes. $\Delta x \cdot \Delta z$ is the projection of this area on the x-y plane. The power absorbed by ΔA is then found by integrating eq (D1).

$$P = \frac{R_s\delta}{2} \int_{\Delta A} \text{Re}\left[-H_\mu^* \frac{\partial H_\mu}{\partial \xi} - H_\upsilon^* \frac{\partial H_\upsilon}{\partial \xi}\right] dA \tag{D2}$$

which can be put in a quasi-differential form resembling eq (D1),

$$\frac{d^2P}{dz \cdot d\tau} \equiv \frac{R_s\delta}{2} \left\langle \text{Re}\left[-H_\mu^* \frac{\partial H_\mu}{\partial \xi} - H_\upsilon^* \frac{\partial H_\upsilon}{\partial \xi}\right] \right\rangle \frac{\Delta A}{\Delta z \cdot \Delta \tau} \tag{D3}$$

where the caret brackets stand for a surface average (the integral in eq (D2) divided by ΔA). Equation (D3) applies either to a "y = constant" wall (τ = x) or a "x = constant" wall (τ = y). The average should extend over at least 10 σ (σ is the rms surface roughness) to be valid. In the present case, the surface roughness of the internal horn surfaces is 10 μcm, easily small enough to make the quasi-differential useful even inside the WR10 waveguide lead of the horn.

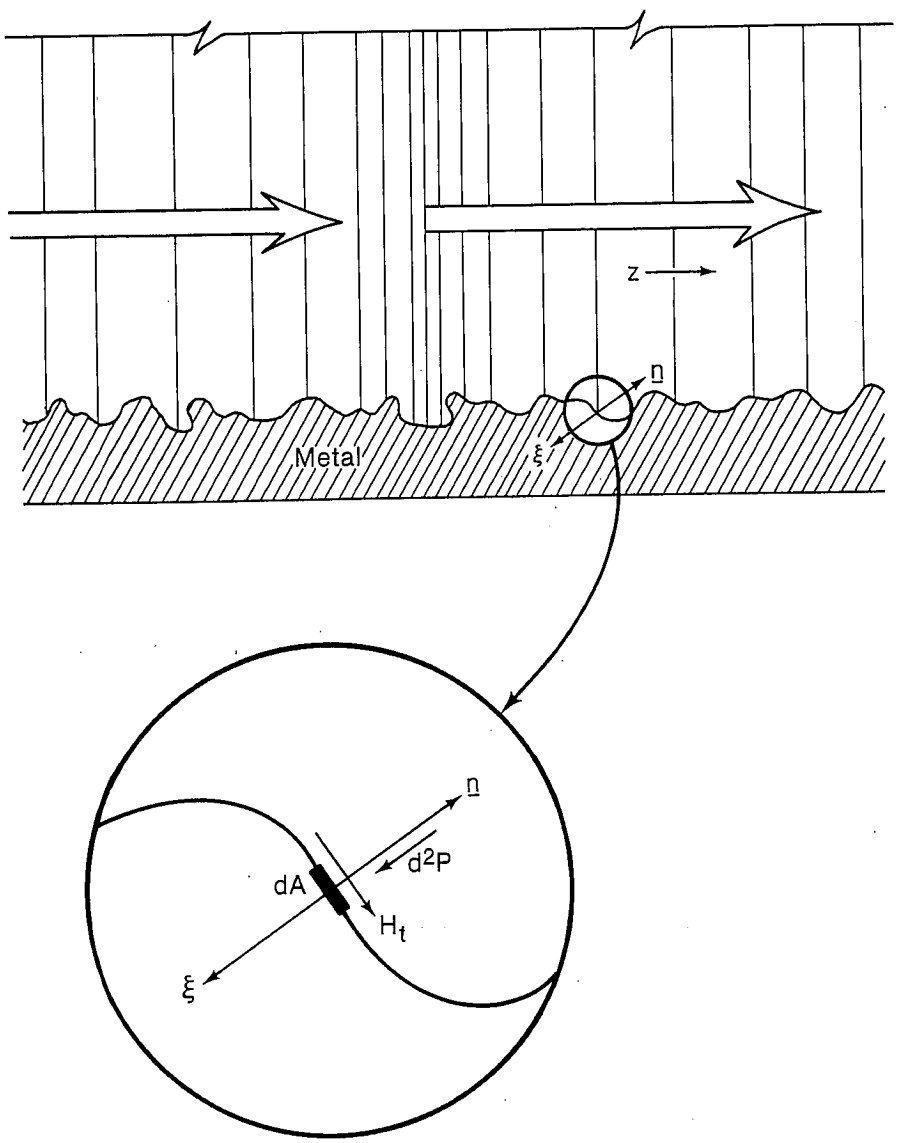

Figure 14. Schematic diagram of an electromagnetic wave traveling along a rough surface.

For locally flat surfaces [29]

$$\mathrm{Re}\left[-H_\mu^* \frac{\partial H_\mu}{\partial \xi}\right] = \frac{|H_\tau|^2}{\delta} \tag{D4}$$

$$\mathrm{Re}\left[-H_\upsilon^* \frac{\partial H_\upsilon}{\partial \xi}\right] = \frac{|H_z|^2}{\delta} . \tag{D5}$$

The terms on the right of these equations are approximations associated with a first-order (in the skin depth) solution for the fields at a metal surface where H_τ (H_x or H_y) and H_z are the incident fields. It is then convenient for the rough surface to define

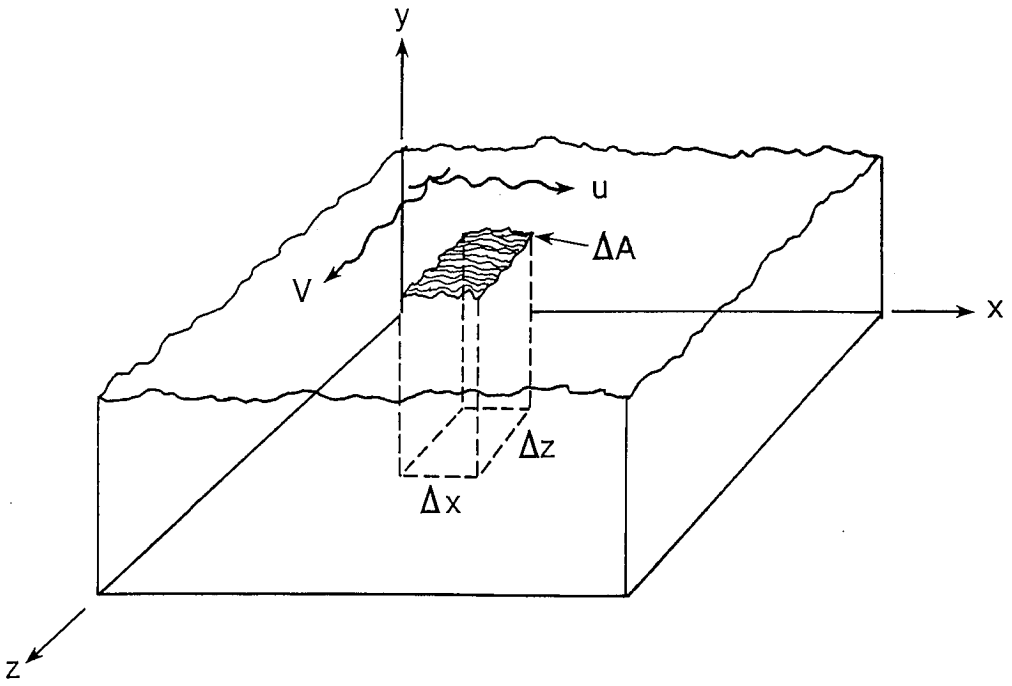

Figure 15. Schematic diagram for the coordinates of a rough surface.

$$K_z \equiv \frac{\langle \mathrm{Re}\left[- H_\mu^* \, \partial H_\mu / \partial \xi \right] \rangle}{|H_\tau|^2 / \delta} \, C \tag{D6}$$

$$K_\tau \equiv \frac{\langle \mathrm{Re}\left[- H_\upsilon^* \, \partial H_\upsilon / \partial \xi \right] \rangle}{|H_z|^2 / \delta} \, C \tag{D7}$$

where

$$C \equiv \frac{\Delta A}{\Delta z \cdot \Delta \tau} \, . \tag{D8}$$

K_z is associated with the surface current containing a z component while the current associated with K_τ is contained entirely in the x-y plane. These two factors are expected to yield the same magnitude [9, 10] if the surface roughness in the z and transverse directions is the same. Furthermore, if the fields on the rough surface could be found to first-order in the skin depth, it is not unreasonable to expect the partial derivatives in eqs (D6) and (D7) to contain a factor δ that would cancel the δ's in these equations. Therefore, K_z and K_τ should depend on the frequency and the surface geometry and be independent of the surface conductivity contained in the skin depth (and thus the temperature).

For wavelengths much greater than the surface roughness, calculations [31] indicate that the K factors lie between unity and the constant C by which the real area is increased over the projection of the area on a plane parallel to the real surface and that they approach C as the frequency increases (or the skin depth decreases). Then, the ratios multiplying the constant C in the equations lie between C^{-1} and unity, approaching unity as the frequency increases. This behavior suggests that the ratios are a measure of what fraction of the rough surface is available or "above cutoff" to the incident fields. Therefore, since there is nothing in this description to suggest a

dependence on anything but the frequency and surface geometry (roughness), it is concluded that the K factors are constant as long as the surface roughness and frequency remain constant. This conclusion is the basic justification for determining the surface roughness factor for the horn by the method described in section 2. Incidentally, this interpretation of the behavior of the ratios explains why the effects of surface roughness increase with frequency (becoming important in the millimeter-wave bands), an insight apparently missing from the literature.

Combining eqs (D2), (D6), and (D7) leads to

$$\frac{d^2P}{dz \cdot d\tau} = \frac{R_s}{2}\left(K_z |H_\tau|^2 + K_\tau |H_z|^2\right) \tag{D9}$$

$$= K \frac{R_s}{2}\left(|H_\tau|^2 + |H_z|^2\right) \tag{D10}$$

where eq (D10) holds when the surface roughness is isotropic and K_z and K_τ both equal the same constant K. Proceeding from eq (D10) by the usual method [25] gives an efficiency

$$\eta = e^{-2K \int a' d\tau} \tag{D11}$$

in place of eqs (C9) and (C10).

Appendix E: Higher-mode contamination

The noise temperature T_n of a lossless waveguide with gradually increasing transverse dimensions that is terminated by a reflectionless absorber at its larger end can be expressed as

$$T_n = T_m + T_m \sum_E \alpha_{ij} + T_m \sum_M \alpha_{ij} \tag{E1}$$

where T_m is the absorber temperature. The first term represents the noise power contained in the dominant (TE_{10}) mode that propagates the entire length of the waveguide without attenuation. The second and third terms represent noise in the higher TE and TM modes, respectively, which are attenuated in the smaller end of the guide. The efficiency factors are related to the increasing transverse dimensions (a and b) of the waveguide and the wavelength λ [25] by

$$\alpha_{ij} = e^{-\int_o^{\ell_{ij}} a_{ij} dz} \tag{E2}$$

where

$$a_{ij} \equiv 2\pi\left(\frac{i^2}{a^2} + \frac{j^2}{b^2} - \frac{4}{\lambda^2}\right)^{1/2} . \tag{E3}$$

The integral is taken from "o" at the small end of the waveguide to that point ℓ_{ij} where the respective mode is propagating.

From eq (E1), the relative uncertainty in the noise temperature due to the presence of incompletely attenuated higher modes at the small end of the waveguide is

$$\frac{\Delta T_n}{T_n} = \sum_2^\infty \alpha_{io} + \sum_1^\infty \alpha_{oj} + 2 \sum_1^\infty \sum_1^\infty \alpha_{ij} . \tag{E4}$$

This equation is applied to the horn in figure 2 from the waveguide flange to the aperture, where a and b are allowed to expand to conform to the transverse horn dimensions. The error depends on the length x_1 of the waveguide portion of the horn as shown in figure 16, where it is seen, that for the horn with an x_1 of 0.31 cm, the error is 0.12%. Thus, if a detector at the output of the standard could respond to all of the modes, it would measure a noise temperature 0.12% higher than T_m.

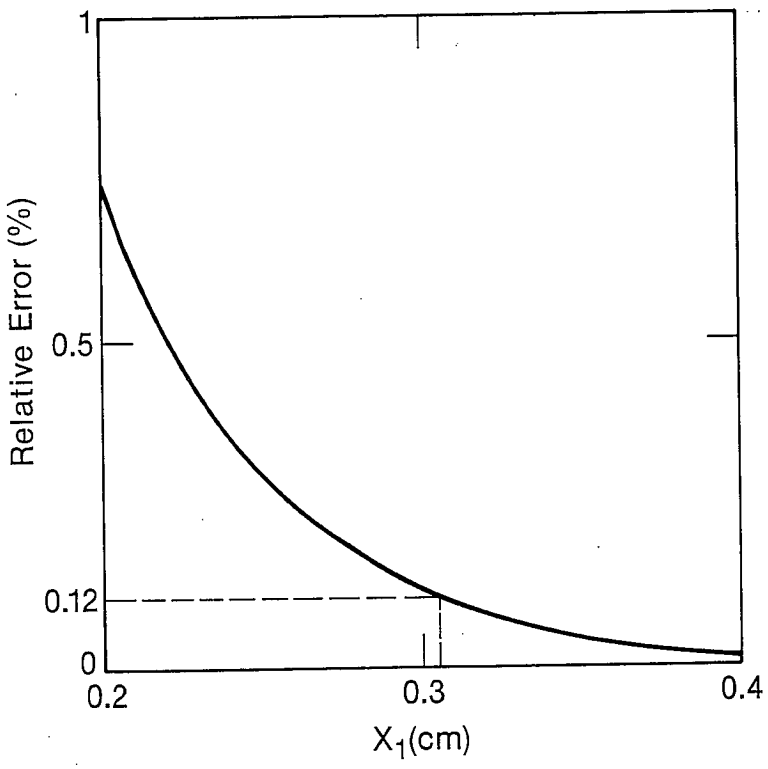

Figure 16. Higher-mode noise-temperature error at 110 GHz for the WR10 horn antenna.

Appendix F: Cavity-radiation error

The excess temperature (eq (3)) is derived on the assumption that the cavity walls and absorber (fig. 7) are at the same temperature T_m, leaving just the antenna noise contribution. Therefore, since the wall temperature varies from T_m up to room temperature, eq (3) predicts too small a correction and is in error. An upper bound to the magnitude of the error is estimated in this appendix. The model of the cavity to be used in the estimate is shown in figure 17, which is an enlarged portion of the assembly drawing in figure 7. The heavy, superimposed lines indicate the confines of the model in this profile view. The horn antenna is represented by lines O-1 and O-2, where the matching quarter-rounds have been deleted to make the calculation easier and to give a more conservative estimate of the error. The cavity walls consist of lines A-B-C-D and G-H-I-J. The real absorber (the wedges) is replaced by the fictitious surface D-E-F-G from which the absorber radiation is assumed to originate. The absorber temperature is T_m, while the walls vary in temperature from T_m at D and G to room temperature at C and H. The rear portion of the walls, A-B-C and H-I-J, are at room temperature. The absorber is reflectionless, while the walls and horn exterior have emissivities [32,33] that vary with temperature.

The sectional view of the standard shown in figure 17 is in the E-plane of the horn, where points 1 and 2 are at the center of the E-edges. In this plane, the sources of radiation in the walls and absorber are included in the heavy lines of the figure. Since the walls of the cavity are metallic, a three-dimensional pattern of images of each source is set up, the source and its images both radiating energy into the horn. To make the image pattern easier to construct, the cavity is assumed to have a square (rather than circular) cross section, restricting the images of a particular source to the plane of the figure and to a plane perpendicular to the figure. The calculations are simplified (and the error made more conservative) by rotating the images in the perpendicular plane by 90° into the plane of the figure. A further simplification is gained by translating the rotated images until each lies directly on top of its nearest neighbor. This last operation doesn't have a great effect on the results, and permits the rotated images to be accounted for by simply doubling the strengths of the images originally in the plane of the figure. The UTD [8] is then applied to the resulting patterns, two examples of which are illustrated in figures 18 and 19. In figure 18 the source is an element of the absorber, and can be seen from the throat area of the horn and the two horn edges, as indicated by the dashed lines connecting the source to these points. The images, on the other hand, can only be seen by the edges. The number of images is infinite, and appear to collect on the condensation line as the images get further away from the edges. In figure 19, the source is in the upper wall behind the horn aperture and, with its images, can only be seen by the upper E-edge. The images in both figures are drawn as though the horn were not present to simplify the drawings and the subsequent calculations. This simplification is not expected to have a large effect on the results since, because of the rectangular horn geometry and circular cavity geometry, no resonance structure is set up behind the horn.

For the source shown in figure 18, the UTD [8] approximation leads to a first-order magnetic field H at point o of the form (for the source in figure 19, only the second term and the first infinite series would be present)

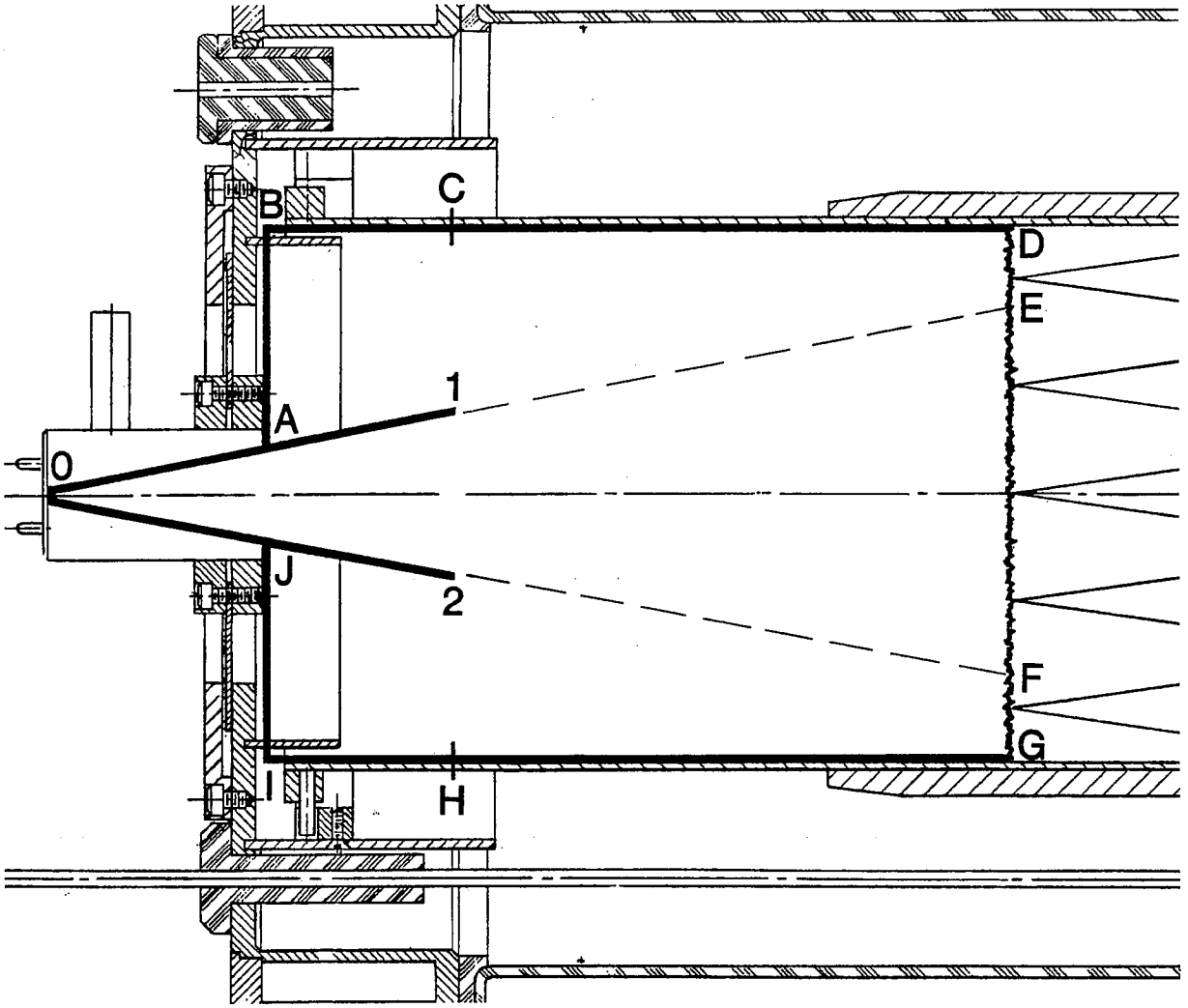

Figure 17. Enlarged view of the WR10 noise-standard assembly drawing showing the outline of the cavity model.

$$H = H_o \frac{e^{-jkr_o}}{kr_o} + H_1(o) \frac{e^{-jkr_1}}{kr_1} (1,o) + H_2(o) \frac{e^{-jkr_2}}{kr_2} (2,o)$$

$$+ 2 \sum_{1}^{\infty} Z_{1i} H_1(i) \frac{e^{-jkr_1(i)}}{kr_1(i)} (1,i)$$

$$+ 2 \sum_{1}^{\infty} Z_{2i} H_2(i) \frac{e^{-jkr_2(i)}}{kr_2(i)} (2, i) . \qquad \text{(F1)}$$

The first term is the field that comes directly from the source at distance r_o. The absence of an infinite series associated with the field H_o indicates that the images are not seen from point o. The second term is the portion of the source field incident on the first edge that is diffracted

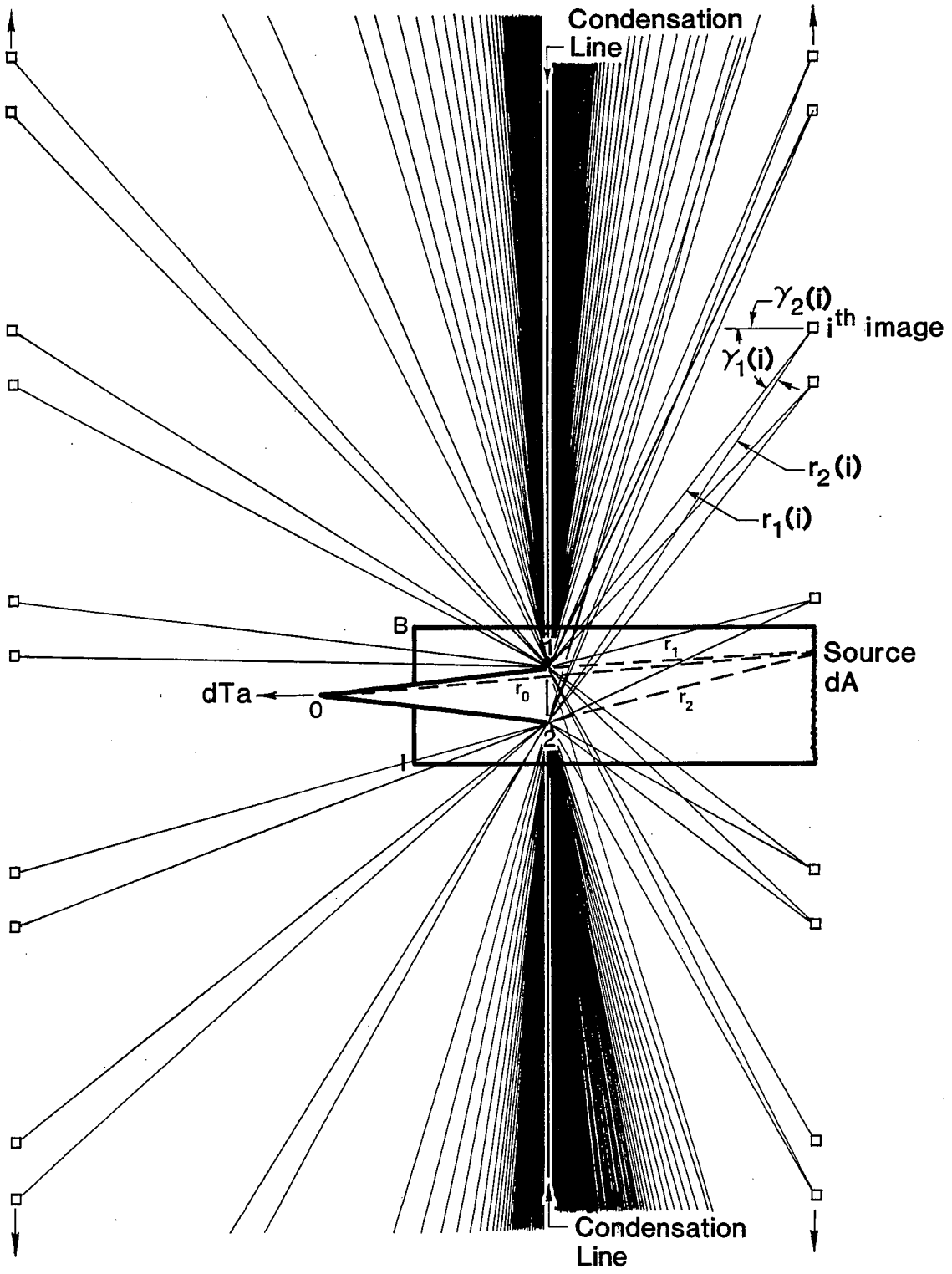

Figure 18. Image pattern of a source in the absorber.

((1, o) is the diffraction coefficient) by the edge to the point o. The third term has a similar interpretation, and the two infinite series (the factor of 2 comes from the image doubling mentioned earlier) are the image fields diffracted to point o. The Z-symbols under the sum signs are the

compound reflection coefficients associated with the multiple reflections of the source in the cavity walls that produce the images. For example,

$$Z_{1i} = \prod_{j=1}^{n_i} z_{1i}(j) \qquad \text{(F2)}$$

is the compound reflection coefficient associated with the i^{th} image as seen by edge 1. The lowercase z's are the reflection coefficients [33] for the individual wall reflections which are n_i in number. The symbol after the "equal" sign signifies that a product of the individual coefficients is calculated. The various z's (indicated by the j in the argument) contain a small amount of wall attenuation, and differ from each other because this attenuation is a function of the wall temperature. The individual back and side wall coefficients differ because of the different angles of incidence of the fields from the source.

The magnitudes H_o, $H_1(o)$, . . . , appearing in eq (F1) are stochastic variables [21] which, when multiplied together and averaged over an ensemble of systems identical to the actual system, yield the source strengths of the radiation from the source or its images. This product takes the general form

$$\langle H_m(i)\, H_n(j)\rangle = C[\varepsilon(\gamma_m(i))\, \varepsilon(\gamma_n(j))\, \cos\gamma_m(i)\, \cos\gamma_n(j)]^{1/2}\, \kappa T B\, k^2\, dA\, K_{mn}(i, j) \qquad \text{(F3)}$$

where m and n denote the edge (1 or 2), and i and j denote the source (o) or an image (1, 2, . . .). ε is the emissivity which depends on the angle of incidence, κ is Boltzmann's constant, T is the temperature of the source, B is the frequency bandwidth of the system to which the noise standard is attached, k is the wavenumber, and dA is the elemental area of the source. The γ's are angles of incidence (fig. 18) , and C is the constant

$$C \equiv \frac{2}{\lambda^2 Z_o} \qquad \text{(F4)}$$

where λ is the wavelength, and Z_o is the free-space impedance.

$$K_{mn}(i, j) \equiv \begin{cases} 1, \text{ cavity walls} \\ \cos(\gamma_m - \gamma_n) \text{ , load} \\ 0, \text{ different sources and source images} \end{cases} \qquad \text{(F5)}$$

Equation (F3) was derived in the ray-optical approximation by using Kirchhoff's law of radiation [34] and Poynting's vector. The emissivities are calculated from the reflectivity [32,33] of the walls, and are equal to unity for the absorber.

The elemental noise temperature dT_n resulting from a particular source and its images is calculated from

$$dT_n = \frac{C' \langle H\ H^* \rangle}{\kappa B} \qquad \text{(F6)}$$

where C' is a constant related to the transformation of the throat field H into the TE_{10} mode fields in the waveguide lead of the horn. When eq (F1) is inserted into (F6) and eq (F3) is applied to the resulting products, there emerges an expression of the form

$$dT_n = C\ C'\ T \{\ \}\ dA \qquad \text{(F7)}$$

where the bracket contains what is left of the product H H*.

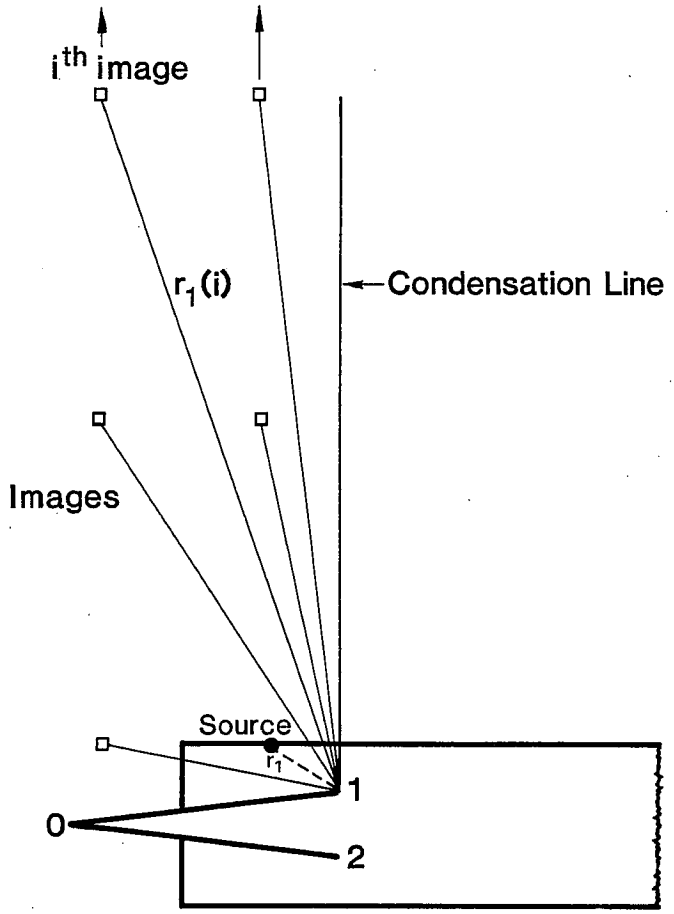

Figure 19. Image pattern of a source in the side wall.

The process just described is relatively simple because it was initiated in the E-plane section of the horn and cavity, the same calculation in any other plane being prohibitively complicated.

However, in other planes, eq (F7) overestimates the effects of the cavity walls on the error because the wall contributions are strongest in the E-plane (since the diffraction is strongest in the center of the E-edges). Thus, if eq (F7) is applied to all sections around the axis of the horn and cavity (that is, if azimuthal symmetry is assumed), the error will be overestimated and conservative. The resulting equation has the form

$$T_n = C\,C' \int T\,\{\,\}\,dA \tag{F8}$$

where the integral is over the surface of the cavity. T and { } are independent of the azimuthal angle, and dA can easily be expressed in spherical coordinates. The terms in the bracket are a function of the wall temperature since the conductivity of the walls depends on temperature. In thermal equilibrium, T_n and T must both equal the absorber temperature T_m, allowing the product C C' to be easily calculated.

$$C\,C' = \left(\int \{m\}\,dA\right)^{-1} \tag{F9}$$

where the m in the brackets is a reminder that, in this case, the bracket is evaluated with the wall temperature set equal to the absorber temperature. The antenna noise temperature now becomes

$$T_n = \frac{\int T\,\{\,\}\,dA}{\int \{m\}\,dA}\,. \tag{F10}$$

The nonisothermal wall-radiation error corresponding to eq (F10) is

$$\frac{\Delta T_n}{T_n} \equiv \frac{T_m - T_n}{T_n}\,. \tag{F11}$$

A computer program written to estimate this error produced the result

$$\frac{\Delta T_n}{T_n} = -\,0.059 - 0.035 = -\,0.094\% \tag{F12}$$

where the first component of the error (0.059) comes from the front portion (C-D and GH in figure 17) of the cavity wall and the second from the back portion (C-B-I-H).

Radiation can leak into the cavity around the radiation shields (6C and 6E in figure 7), and possibly around the membrane (17). Because of the millimeter-wave absorber (16) underneath the load holder (14), the radiation leaking around the shields has a radiation temperature [16] only 2 K greater than T_m, and causes an additional error no greater than - 0.001%. The radiation possibly leaking around the membrane has a radiation temperature equal to room temperature, and causes an additional error no larger than - 0.01%. Thus, the total error due to the leakage and the walls is - 0.10% (- 0.001 - 0.01 - 0.094).

Appendix G: Multiple reflections

Multiple reflections taking place between the horn aperture and the back wall of the cavity cause an error in the calculated noise temperature since the derivation (Appendix A) of eqs (3) and (5) assumes a reflectionless cavity. These reflections modify both the horn and cavity-wall contributions to the noise temperature of the standard. The magnitude of the error due to the changes in the horn-generated noise can be found by determining that portion of the reflection coefficient of the standard that is a result of back-wall reflections. This was done by measuring the change in the reflection coefficient of the horn waveguide port between the configuration shown in figure 7, and the configuration with the horn, load holder (14), and load (13) in place and all other items in the figure removed. The resulting change in magnitude was 0.001. An expression for the relative noise temperature error is derived by considering the horn as a two-port junction [35], terminated by a load at temperature T_m whose reflection coefficient changes from 0 to 0.001.

$$\frac{\Delta T_n}{T_n} = 2|\Gamma|^2 \frac{\Delta T}{T_m} \tag{G1}$$

where ΔT is the excess noise temperature and is estimated from eq (3) and figure 5 to be approximately 2 K (T_m and T_o are approximately 77 K and 300 K, respectively). Completing the calculation in eq (G1) shows this part of the error to be completely negligible.

An upper bound to the error in neglecting the excess noise generated by the cavity walls is carried out in Appendix F, where the effects of multiple reflections are ignored. However, since the rear cavity wall is so highly reflecting, it is reasonable to expect that the excess noise is underestimated (a tighter coupling to the cavity can only increase the noise as the cavity walls have a higher temperature than the absorber) by this zero-order approximation. A first-order approximation can readily be obtained by considering the additional noise from the E-edge images. Furthermore, after the first order, the effects of higher-order edge images of the edges fall off rapidly. Figure 20 illustrates a pattern of source images with the addition of images from both E-edges, the crosses representing the upper edge and the asterisks the lower edge. The source and each of its images excites either half or all of the edge pattern, depending on the location of the source or its images. Using the UTD, the edge images lead to an enhanced magnetic field H' in the horn throat (the symbols are described in Appendix F).

$$H' = H + 2 \sum_{j=1}^{\infty} \frac{H_1(o)}{2} \frac{e^{-ikr_1}}{kr_1} (1, o, j)\, Z_{3j}(1, j) + 2 \sum_{j=1}^{\infty} \frac{H_2(o)}{2} \frac{e^{-jkr_2}}{kr_2} (2, o, j)\, Z_{4j}(2, j)$$

$$+ 2 \sum_{j=1}^{\infty} 2 \sum_{i=1}^{\infty} Z_{1i} \frac{H_1(i)}{2} \frac{e^{-jkr_1(i)}}{kr_1(i)} (1, i, j)\, Z_{3j}(1, j)$$

$$+ 2 \sum_{j=1}^{\infty} 2 \sum_{i=1}^{\infty} Z_{2i} \frac{H_2(i)}{2} \frac{e^{-jkr_2(i)}}{kr_2(i)} (2, i, j)\, Z_{4j}(2, j) \tag{G2}$$

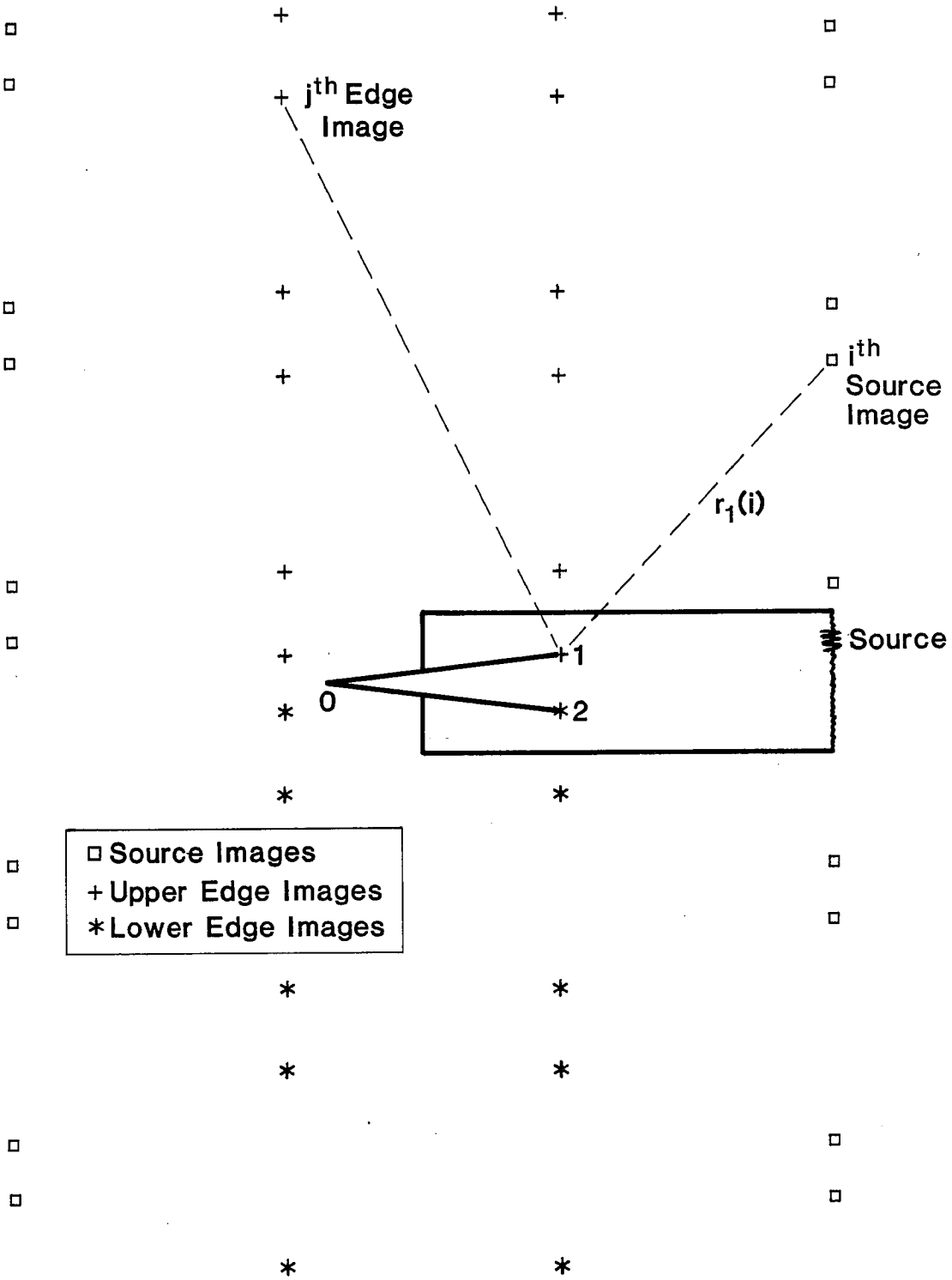

Figure 20. Image pattern of a source in the absorber and the excited E-edges.

where H is the original field (eq (F1)). The factor 2 dividing the source strengths is a result of normalizing the previous equations for grazing incidence [8]. The only new symbols are the triplets like the (1, i, j) in the four series of edge fields. This new diffraction coefficient describes the excitation (fig. 20) at the j^{th} edge image by the source image at position "i." Similar

interpretations apply to the other coefficients. Proceeding as in Appendix F, the noise temperature T_n' that now includes first-order reflections has the form (c.f. eq (F8))

$$T_n' = C\,C' \int \{\ \}\ dA + 4\,S\,C\,C' \int T\,[\ ]\ dA \tag{G3}$$

where S is a constant (close to unity) that is the result of the approximations made to arrive at the equation. The symbol [ ] bears the same relationship to the additional terms in H' that the symbol { } bore to H in eq (F1). Again, using the second law of thermodynamics,

$$C\,C' = \left(\int \{m\}\ dA + \int [m]\ dA \right)^{-1}\ , \tag{G4}$$

where the m in the brackets indicates that they are evaluated at the absorber temperature T_m. Combining eq (G3) and (G4),

$$T_n' = T_n \left(\frac{1 + 4\,S \int T\,[\ ]\ dA / \int T\,\{\ \}\ dA}{1 + 4\,S \int [m]\ dA / \int \{m\}\ dA} \right)\ . \tag{G5}$$

With the help of a computer program,

$$\frac{\Delta T_n}{T_n} \equiv \frac{T_n - T_n'}{T_n} = -\ 0.054\% \tag{G6}$$

is the resulting error in the output noise temperature due to neglecting the next higher-order (first-order multiple reflection) contribution of the excess noise generated by the cavity walls. Comparing this with eq (F12) shows that the first-order multiple reflection is not insignificant compared to the zero-order calculation.